Hydrodynamic characterization of Gyroid, Diamond and Split-P Triply Periodic Minimal Surfaces as porous medium

International Journal of Heat and Mass Transfer 252 (2025) 127439

Contents lists available at ScienceDirect

International Journal of Heat and Mass Transfer

journal homepage: www.elsevier.com/locate/ijhmt

Hydrodynamic characterization of Gyroid, Diamond and Split-P Triply Periodic Minimal Surfaces as porous medium

E. Gajetti [a], G. Boccardo [b], L. Savoldi [a], L. Marocco [c,*]

[a] Politecnico di Torino, Dipartimento Energia "Galileo Ferraris", Corso Duca degli Abruzzi 24, 10129 Torino, Italy
[b] Politecnico di Torino, Department of Applied Science and Technology, Corso Duca degli Abruzzi 24, 10129 Torino, Italy
[c] Politecnico di Milano, Department of Energy, via Lambruschini 4, 20156 Milano, Italy

ARTICLE INFO

Keywords:
Triply Periodic Minimal Surfaces (TPMS)
Darcy-Forchheimer equation
Permeability
Inertial drag
Computational Fluid Dynamics (CFD)
Hydraulic characteristics

ABSTRACT

Triply Periodic Minimal Surfaces are gaining significant attention as engineered porous media for applications in fluid transport and thermal management systems due to their unique geometric properties. However, accurate prediction of pressure drop across TPMS structures remains a challenge, particularly in transitioning flow regimes. This study addresses this gap by investigating the hydrodynamic behavior of Gyroid, Diamond, and Split-P geometries using computational fluid dynamics simulations across a range of Reynolds numbers, from viscous to weakly inertial regimes. Two modeling frameworks were utilized: the Ergun equation, commonly used for packed beds, and the Darcy-Forchheimer equation, enhanced with newly developed correlations for permeability and inertial drag factor. An adapted Kozeny-Carman equation was also applied for permeability prediction. The developed correlations, expressed as power-law functions of porosity and tortuosity, demonstrated high accuracy, with relative errors below 10 % for most configurations and a maximum error of 21 % for the more complex Split-P1 geometry. Validation in larger-scale geometries, such as pipes filled with TPMS, confirmed the scalability and robustness of the proposed models, even when accounting for variations in the hydraulic diameter due to wall effects. The results demonstrate the superior suitability of the Darcy-Forchheimer equation with the developed permeability and inertial drag factor models, particularly for complex geometries like Split-P. In contrast, the Ergun equation fails to accurately predict pressure drop across the investigated TPMS, underscoring its limitations for these geometries. Furthermore, while the inclusion of tortuosity in the correlations provides additional detail, it does not offer significant advantages over the simpler permeability-porosity relation for any of the investigated TPMS, making the latter a more practical choice for design and optimization applications in systems such as heat sinks and porous flow devices

1. Introduction

First described in the late 19th century [1], Triply Periodic Minimal Surfaces (TPMS) represent a family of surfaces characterized by zero mean curvature and a three-dimensional periodic structure extending in all directions. Their complex and continuous geometry provides a high specific surface area that enhances heat transfer efficiency while maintaining a low pressure drop. Recent advancements in additive manufacturing have enabled the precise fabrication of TPMS structures, which have earned significant attention for their potential in optimizing thermal management and fluid flow applications. These surfaces can be configured as solid-TPMS with single-channel networks for applications such as heat sinks [2,3] or as sheet-TPMS with multi-channel configurations, ideal for compact heat exchangers [4–6]. TPMS are well-suited to a range of thermal applications, including latent-heat energy storage [7] and combustion in porous media [8].

Beside studies where the fluid-dynamic behavior of TPMS is investigated just to provide better understanding of the flow path within the lattice or to develop correlations for the pressure drop [9–12], the hydraulic behavior of different TPMS, with the assessment of permeability, is crucial in the design of better scaffolds in tissue engineering. This topic is addressed for instance in [13–15].

The airflow resistivity in TPMS lattice structures is investigated as one of the key factors determining the sound absorption characteristics in situations where those structures are used to enhance acoustic comfort [16].

The investigation of the pressure drop across a TPMS lattice can

* Corresponding author.
E-mail address: luca.marocco@polimi.it (L. Marocco).

https://doi.org/10.1016/j.ijheatmasstransfer.2025.127439
Received 21 December 2024; Received in revised form 22 May 2025; Accepted 22 June 2025
Available online 2 July 2025

Nomenclature

Roman letters

A_{wet}	Wetted area (m^2)
A_c	Cross sectional area (m^2)
C_F	Inertial drag factor
c	Iso-surface parameter
D_h	Hydraulic diameter (m)
D_p	Particle diameter (m)
K	Permeability (m^2)
L_c	TPMS cell size (m)
p	Pressure (Pa)
S_V	surface to volume ratio (m^{-1})
$\boldsymbol{u}$	Velocity vector (m /s)
U_s	Superficial velocity (m /s)
U	Velocity magnitude (m /s)
u_y	Velocity in the main flow direction (m /s)
$\overline{u}_y$	Cross-sectional velocity in the main flow direction (m /s)
V	Volume (m^3)

Greek letters

θ	Helicity angle
μ	Dynamic viscosity (Pa s)
ν	Kinematic viscosity (m^2/s)
ρ	Density (kg/m^3)
φ	Porosity
τ	Tortuosity
$\boldsymbol{\Omega}$	Vorticity vector $(1/s)$

Non-dimensional numbers

Re_{Dh}	Reynolds number based on the hydraulic diameter

Subscripts

KC	Kozeny-Carman
rel	Relative
f	Fluid
tot	Total

Operators

$\langle\cdot\rangle_{L_c}$	Average over L_c
$\langle\cdot\rangle_V$	Average over volume
$\lvert\cdot\rvert$	Magnitude

become a viable tool to assess the effect of different manufacturing techniques [17]. Moreover, the analysis of the pure hydraulic behavior of TPMS lattice allows the optimization of flow characteristics as done, for instance, in [18], and it constitutes a mandatory step for the investigation of the thermal behavior of the porous structure in heat sinks or heat exchangers [19] and in transpiration cooling applications [20].

Performing detailed Computational Fluid Dynamics (CFD) simulations of a complete heat sink or heat exchanger equipped with TPMS structures is computationally demanding, particularly when accurate predictions of pressure drop and heat transfer are needed. As a result, developing suitable engineering correlations becomes essential for designing such equipment, allowing reliable performance estimations without extensive simulations. In terms of hydraulic behavior, TPMS have been effectively modeled as structured porous media, as demonstrated in prior literature studies. These models reveal both a viscous regime, governed by Darcy law, and an inertial regime, characterized by extensions such as the Darcy-Forchheimer equation or Ergun law. Such methodologies facilitate broader applications of TPMS in engineering applications by simplifying performance evaluations within larger systems.

Several studies have already been conducted focusing on the viscous (Darcian) regime, primarily aiming to assess the permeability of TPMS and its correlation with porosity. Montazerian et al. [21] numerically examined the longitudinal permeability of various solid-TPMS, including Gyroid and Diamond, and successfully fitted CFD results using both a power law and the Kozeny-Carman relationship. In the latter case, they computed the Kozeny-Carman coefficient as a quadratic function of porosity. Zhianmanesh et al. [22] explored the permeability of different TPMS with both uniform and variable porosity, also including the solid-Gyroid. They developed a power law permeability-porosity correlation for each TPMS they studied, with distinct coefficients and exponents. Lu et al. [23] proposed an exponential law to describe the permeability- porosity relationship for the TPMS they studied, such as solid-Gyroid and solid-Diamond. They found significant discrepancies in the comparison to CFD results when applying the standard Kozeny-Carman equation for permeability without adjusting the coefficients. Additionally, Asbai-Ghoudan et al. [24] numerically computed the permeability in the viscous regime and developed a single correlation for the sheet-Gyroid lattice, relating permeability to an equivalent pore size and porosity ranging from 50 % to 90 %. They also observed that the exponent in the permeability-porosity relationship differs notably between sheet-based and solid-based TPMS architectures.

The behavior of TPMS in the transition from the viscous to the inertial regime, has been analyzed both experimentally and numerically. In experimental studies, Castro et al. [25] tested three constant-porosity sheet-TPMS (Gyroid, Diamond, and Primitive) and observed that the Darcy law no longer applies at high mass flow rates. Later, Tupin and Ohta [26] revisited these findings using the Darcy-Forchheimer law, fitting the data to compute both the permeability and the (inertial) Forchheimer factor, though their analysis was limited to a single porosity value. Piedra et al. [27] performed a CFD study of sheet-Primitive and IWP TPMS, finding that the flow within these structures is well described by Darcy-Forchheimer law. They developed a power law model for permeability and the inertial factor, with predictions showing mean errors of 5–11 % compared to CFD simulations. However, their study was restricted to the above-mentioned analyzed geometries. Ahmed and Bottaro [28] focused on six different sheet-TPMS (among which the Gyroid and the Split-P) at varying porosities and investigated the transition from the viscous to the inertial regime, though they did not attempt to relate permeability to any geometric parameters.

Alternative approaches using the Ergun equation, rather than the Darcy-Forchheimer equation, have also been explored. Hawken et al. [10] found that the original Ergun coefficients were inadequate for TPMS. Consequently, they derived their own set of coefficients by fitting the Ergun equation to experimental data for the solid-Diamond structure at various porosities. Similarly, Cheng et al. [29] conducted a numerical study and found that each TPMS required a different fit for the Ergun equation, with distinct coefficients for each topology they investigated.

From the previous studies, several key insights emerge regarding the relationship between permeability and porosity for TPMS. First, permeability-porosity correlations based on a power law relationship indicate that the exponent tends to be consistent across different solid-type TPMS structures, whereas it differs significantly for sheet-type TPMS. Moreover, within each type (whether solid or sheet), individual TPMS topologies exhibit a distinct fluid-dynamic behavior. As such, each topology must be evaluated individually to determine the appropriate coefficients for use with either Darcy-Forchheimer or Ergun-type correlations.

This study presents an in-depth numerical analysis of three solid-type TPMS topologies, namely Gyroid, Diamond, and Split-P, focusing on their behavior in both viscous and inertial regimes when their porosity varies from 30 % to 60 %. Initially, the suitability of the Ergun equation for predicting pressure drops in these TPMS structures is assessed. Then, the applicability and accuracy of the Darcy-Forchheimer equation is examined, deriving permeability-porosity and inertial factor-porosity correlations across all studied topologies. Furthermore, this framework is extended by incorporating tortuosity, leading to the development of permeability-porosity-tortuosity and inertial factor-porosity-tortuosity correlations, which possibly enhance the predictive accuracy. To validate these findings, initially based on single-cell TPMS simulations, numerical tests are performed within a TPMS-packed tube, simulating realistic heat sink conditions. This approach ensures that the derived correlations are robust and applicable for practical engineering design.

The selection of the three TPMS topologies addressed here was guided by a balance between studying well-established structures in the literature, such as the Gyroid and Diamond, and exploring a relatively unexamined topology, the Split-P. Additionally, our study is restricted to uniform TPMS structures, ensuring that one of the lattice axes aligns with the main fluid flow direction, without any modifications or rotations of the cell. This foundational approach is essential for developing a thorough understanding of the fundamental geometries before expanding to more complex or hybrid configurations. By initially examining the unmodified structures, the development of baseline correlations is targeted, that may later be extended to describe modified or rotated configurations, rather than treating these as entirely separate geometries.

2. Selection of TPMS lattices

This study investigates solid-type TPMS, focusing on three representative topologies: Gyroid, Diamond, and Split-P. These lattices are parameterized by a characteristic length scale L_c, which defines the cell size along the orthogonal axes x, y, and z. All TPMS lattices were generated using the nTop software [30], and the y-axis coincides with the main flow direction.

2.1. TPMS geometries and flow direction

The three TPMS topologies considered are defined by the following set-level functions, where $X = \frac{2\pi x}{L_c}$, $Y = \frac{2\pi y}{L_c}$ and $Z = \frac{2\pi z}{L_c}$:

- Gyroid (Eq. (1)):

$$f(x,\ y,\ z) = \ sin(X)cos(Y) + \ sin(Y)cos(Z) \ + \ sin(Z)cos(X) = c \tag{1}$$

- Diamond (Eq. (2)):

$$\begin{aligned} f(x,\ y,\ z) = {} & sin(X)sin(Y)sin(Z) \ + \ sin(X)cos(Y)cos(Z) \\ & + \ cos(X)sin(Y)cos(Z) + \ cos(X)cos(Y)sin(Z) \\ & = c \end{aligned} \tag{2}$$

- Split-P (Eq. (3)):

$$\begin{aligned} f(x,\ y,\ z) = {} & 1.1 \times (sin(2X)sin(Z)cos(Y) + \ sin(2Y)sin(X)cos(Z) \\ & + \ sin(2Z)sin(Y)cos(X)) - \ 0.2 \times (cos(2X)cos(2Y) \\ & + \ cos(2Y)cos(2Z) + \ cos(2Z)cos(2X)) - \ 0.4 \\ & \times (cos(2X)cos(2Y)cos(2Z)) = c \end{aligned} \tag{3}$$

In the literature, the Diamond lattice is sometimes represented by an alternative formulation (Eq. (4)), derived from Eq. (2) through a suitable rotation of the coordinate axes. This redefinition mismatches the alignment of the main flow direction adopted here (along the y-axis in all cases) with the principal axes of the lattice x', y' and z'. Such a transformation could influence the fluid interaction with the lattice structure, impacting the hydraulic characteristics, so that only the formulation in Eq. (2) has been adopted.

$$f(x',\ y',\ z') = \ cos(X')cos(Y')cos(Z') - \ sin(X')sin(Y')sin(Z') = c \tag{4}$$

2.2. Parameterization and isosurfaces

The porosity φ, defined as the ratio of fluid volume V_f to the total volume V_{tot}, as in Eq. (5), is a key parameter used to describe the structure of the TPMS lattice.

$$\varphi = \frac{V_f}{V_{tot}} \tag{5}$$

Each TPMS lattice is characterized by the isosurface parameter c, which separates the two sub-volumes. If these sub-volumes are interpreted as solid and fluid domains, respectively, a "solid" lattice is generated (the "sheet" lattice is beyond the scope of this study). When $c = 0$, the Gyroid, Diamond, and Split-P lattices have a porosity of 0.5, indicating equal volumes of solid and fluid. However, unlike the Gyroid and Diamond structures, where the fluid and solid domains are fully interchangeable, the Split-P lattice does not exhibit this interchangeability. For the Split-P lattice, the fluid and solid regions are complementary but not equivalent, even at equal partitioning, as shown in Fig. 1. When $c \neq 0$, the ratio of fluid to solid volume changes, leading to different porosities for each lattice configuration.

This study investigates TPMS structures with porosities of 30 %, 40 %, 50 %, and 60 %, analyzing how the void fraction influences fluid dynamics across these solid-TPMS configurations. As mentioned above, the Split-P topology produces two distinct, bi-continuous domains, namely Split-P1 and Split-P2. This effectively doubles the configurations for this topology, resulting in 16 configurations for analysis, as shown in Fig. 1.

2.3. Geometric parameters and their variation with porosity

Key geometric parameters, such as the isosurface parameter c, wetted area, hydraulic diameter, and tortuosity, were examined for their variation with porosity. The parameter c modulates the porosity by shifting the isosurface of the TPMS lattice, adjusting the fluid volume V_f relative to the total volume V_{tot}. As illustrated in Fig. 2a, the porosity varies nearly linearly across the examined range (30 %–60 %), consistently with previous findings by Montazerian et al. [31] and Fisher et al. [32] for the solid Gyroid.

As shown in Fig. 2b, the wetted surface area follows a parabolic trend with porosity, reaching its maximum at 50 %. At this porosity, the volumes of solid and fluid are equal, resulting in the highest possible interface between the two phases. Moving away from this point, either by increasing or decreasing the porosity, leads to a symmetric reduction in the wetted area. For example, configurations with 40 % and 60 % porosity exhibit the same wetted surface. This behavior reflects the symmetry in the solid-to-fluid volume ratio around the 50 % threshold, a trend also reported by Lu et al. [23].

Fig. 2c illustrates the relationship between hydraulic diameter D_h and porosity φ across the different TPMS configurations. The hydraulic diameter D_h can be expressed as in Eq. (6):

$$D_h = 4\varphi\frac{V_{tot}}{A_{wet}} = 4\ \frac{V_f}{A_{wet}} = \frac{4}{S_V} \tag{6}$$

where $S_V = \frac{A_{wet}}{V_f}$ is the surface-to-volume ratio. The increase in D_h with porosity reflects the behavior of S_V. Indeed, as porosity increases, S_V decreases, indicating that the lattice has a lower wetted area relative to the fluid volume. This decrease in S_V at higher porosities corresponds to larger, more accessible flow channels within the structure.

In terms of specific structures, Gyroid exhibits the highest hydraulic diameter across all porosities, which corresponds to its relatively open and interconnected structure, providing broader flow paths compared to the Diamond and Split-P configurations. Diamond shows a moderately

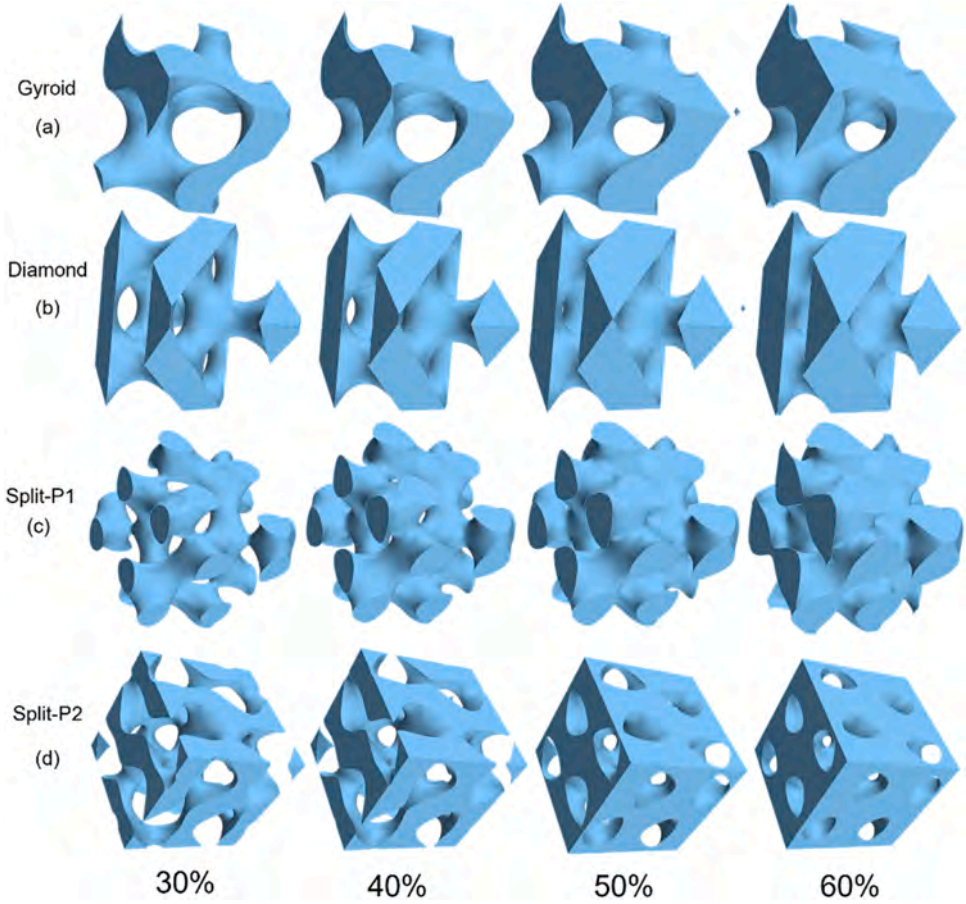

Fig. 1. Fluid volume of analyzed TPMS geometries at 30, 40, 50 and 60 % porosities. a) Gyroid, b) Diamond, c) Split-P1, d) Split-P2.

lower hydraulic diameter. Split-P1 and Split-P2 display identical D_h values at the same porosity due to their complementary domain structures. For example, if Split-P1 at 40 % porosity is considered, Split-P2 at the same porosity has a value of A_{wet} corresponding to that of Split-P1 at 60 % porosity. Given the symmetry in their configurations, implying they have the same A_{wet} at 40 % and 60 % porosity (Fig. 2b), the value of A_{wet} of Split-P2 at 40 % porosity matches the value of A_{wet} of Split-P1 at the same porosity and thus they have the same D_h.

2.4. Tortuosity trends and flow characteristics

The tortuosity τ, defined as in Eq. (7), is expressed as the ratio of the volume-averaged velocity magnitude $\langle U \rangle_V$ to the volume-averaged velocity in the main direction $\langle u_y \rangle_V$, providing insight into the complexity of flow paths within the TPMS. Traditionally, the tortuosity is defined as the ratio of the actual path length to the straight-line distance, focusing on the geometric complexity of flow paths. The velocity-based approach used here is equivalent at low Reynolds numbers ($Re_{Dh} \approx 1$), where viscous forces dominate and flow paths reflect the geometric constraints of the structure [33–36]. Evaluating tortuosity in this regime ensures that it captures intrinsic geometric properties, providing a robust, flow-sensitive measure tied to the lattice structure and unaffected by inertial effects.

$$\tau = \frac{\langle U \rangle_V}{\langle u_y \rangle_V} \tag{7}$$

As shown in Fig. 2d the tortuosity, unlike hydraulic diameter, decreases with increasing porosity across all TPMS structures. This trend suggests that as porosity increases, the fluid pathways within the lattice become less convoluted, offering more direct flow channels. However, the rate and pattern of tortuosity reduction vary between the structures, reflecting differences in their geometries.

For Diamond, Gyroid, and Split-P 2, tortuosity decreases nearly linearly as porosity increases. This linear decrease suggests a gradual simplification of flow paths as the fluid domain expands, making it easier for fluid to traverse the structure with fewer directional changes or obstructions. In these structures, the tortuosity reduction follows a predictable pattern, with Diamond consistently showing the highest tortuosity across the porosity range, indicating more intricate flow paths, and Gyroid exhibiting intermediate values. In contrast, Split-P1 displays an almost parabolic relationship between tortuosity and porosity over the observed range. At lower porosities (around 30 %), Split-P1 shows a higher tortuosity compared to Split-P2, but as porosity increases, tortuosity drops more sharply, eventually converging to similar values as Split-P2 at higher porosities (around 60 %). This parabolic trend indicates a more rapid transition from complex to streamlined flow paths within the Split-P1 configuration, suggesting that its geometric structure undergoes a pronounced change in flow behavior as porosity increases.

These observations underscore the importance of the tortuosity as an indicator of fluid flow complexity within TPMS lattices. While the hydraulic diameter provides consistent scale information across configurations, the tortuosity highlights differences in the flow field. Previous studies by Dolamore et al. [37] and Gado et al. [38] found similar hydraulic diameter and tortuosity values for Gyroid and Diamond structures. Such insights emphasize that simplified models relying only on hydraulic diameter or porosity could be insufficient to capture the complexities of fluid flow in TPMS structures. Detailed pore-scale analyses are essential to fully understand how tortuosity, specific structural features, and porosity interact to influence flow dynamics.

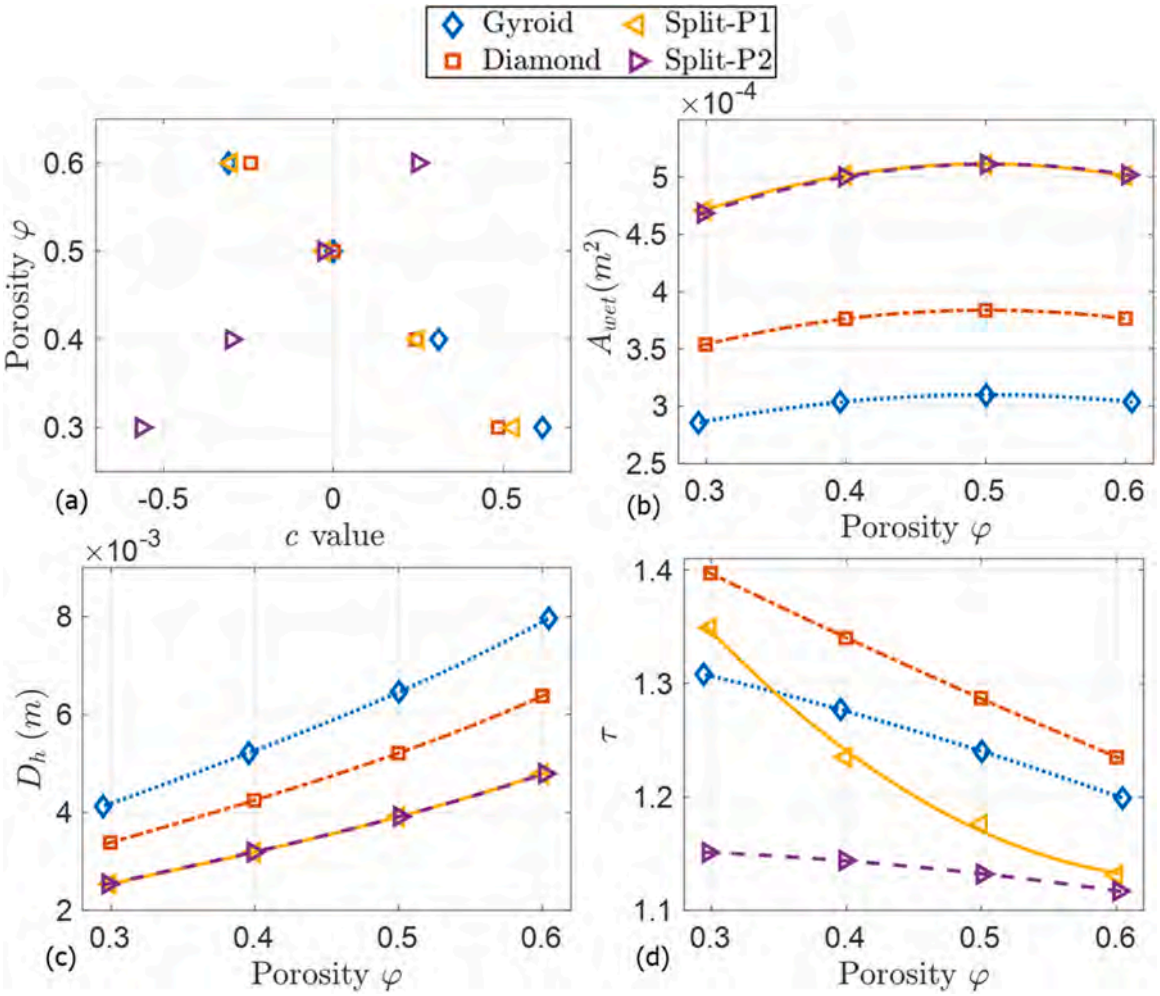

Fig. 2. Variation of geometric parameters for the investigated TPMS: (a) Porosity φ vs. isosurface parameter c, (b) wetted surface A_{wet} vs. φ, (c) hydraulic diameter D_h vs. φ, (d) tortuosity τ vs. φ.

3. Computational methodology and simulation setup

This section describes the computational framework and simulation strategies employed to analyze the flow characteristics within TPMS structures. The methodology refers to a single TPMS unit cell, representing an infinite periodic medium. This approach allows for the development of predictive pressure drop correlations for individual TPMS structures, which are later validated in larger, more complex configurations comprising multiple unit cells.

3.1. Computational domain, boundary conditions, and Reynolds number range

In this study, each TPMS geometry is simulated within a single periodic unit cell of size $L_C = 10$ mm. As shown in Fig. 3, periodic boundary conditions are applied to eliminate boundary effects and enforce a pressure drop along the main flow direction, while maintaining zero transverse pressure gradients. This setup allows a fully developed flow field across the cell, with velocity variations occurring internally but not across the boundary faces. Similar approaches have been used in prior studies [39].

The simulations cover a range of Reynolds numbers from 0.3 to 100, calculated based on the hydraulic diameter D_h (Eq. (8)),

$$Re_{D_h} = \frac{D_h U_P \rho}{\mu} = \frac{D_h U_s \rho}{\mu \varphi} \tag{8}$$

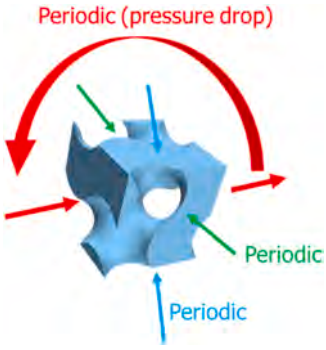

Fig. 3. Periodic boundary conditions on the boundary faces and pressure drop enforced across inlet and outlet faces.

In the above equation, ρ is the fluid density, μ the dynamic viscosity and U_p is the pore velocity, calculated as the superficial velocity U_s divided by the porosity φ. The superficial (or Darcian) velocity U_s is defined as the volume flow rate $\dot{V}$ divided by the total cross sectional area of the unit cell as in Eq. (9).

$$U_s = \frac{\dot{V}}{L_c^2} \tag{9}$$

3.2. Numerical model, solver configuration and mesh uncertainty

The Reynolds numbers span both viscous and inertial regimes, remaining well within the range where turbulent effects are negligible, i.e. approximately $Re_{Dh} < 300$ [40]. The steady-state, incompressible Navier-Stokes equations for laminar flow are solved for an isothermal, Newtonian fluid. The continuity and momentum equations are discretized and solved using OpenFOAM v2212, where pressure-velocity coupling is managed via the SIMPLE algorithm. Convective terms are discretized using a linear upwind scheme, while a central difference scheme is applied to the diffusive terms. This setup ensures accuracy and stability across the entire range of Reynolds numbers analyzed.

Polyhedral meshes without boundary layers were generated using STAR-CCM+ (version 17.02.008-r8). Four progressively refined grids were prepared to evaluate the numerical error and assess the reliability of the simulation results for the 30 % porosity configurations, where the highest velocity values are expected for a given flow rate. The corresponding cell counts for each grid are reported in Table 1, and visualizations of the surface meshes are shown in Fig. 4.

The uncertainty analysis followed the guidelines of the ASME V&V 20–2009 standard [41] to ensure rigorous evaluation of the numerical accuracy. The study employed a systematic grid refinement approach to estimate discretization errors and compute numerical uncertainties. The analysis was based on the finest grid (Grid 1), as presented in Table 1, with all computed numerical uncertainties falling below 5 % for the volume-averaged velocity magnitude at the highest investigated Reynolds number $Re_{Dh} \sim 100$. These results validate the robustness of the selected mesh configuration. The refinement study revealed that the Gyroid structure, being less intricate, requires fewer cells to capture its flow features accurately compared to the Split-P structures, which are the most geometrically complex. The finest mesh (Grid 1) was subsequently employed for all simulations at 30 % porosity. The same grid generation strategy was applied to other porosity values, providing a uniform level of detail and a conservative estimation of the accuracy in all cases.

4. Results and discussion

4.1. Velocity distribution analysis

Fig. 5 presents the velocity distribution, normalized to the maximum inlet velocity, in the main flow direction for Gyroid, Diamond, Split-P1 and Split-P2 at 50 % porosity, comparing low ($Re_{Dh} \sim 0.3$) and high ($Re_{Dh} \sim 100$) Reynolds numbers. At low Reynolds numbers, all TPMS structures exhibit smooth, stable flow profiles, indicating that viscous forces dominate. As Reynolds number increases to $Re_{Dh} \sim 100$, the velocity profiles become more complex, reflecting the influence of inertial forces. In the Gyroid structure, localized regions of negative velocity can be observed, indicating minor flow separation or reversal near specific surfaces, which indicates increased flow complexity due to inertial effects. The Diamond structure, however, maintains a relatively uniform velocity distribution even at $Re_{Dh} \sim 100$, demonstrating a more stable flow regime with little evidence of separation.

The Split-P1 and Split-P2 structures exhibit much greater flow complexity at $Re_{Dh} \sim 100$, with significant velocity variations, including wider areas of negative velocity, which denote flow reversal. The intricate geometry of the Split-P structures seems to enhance inertial effects, leading to more complex flow patterns and greater variation in velocity profiles.

Table 1
Number of polyhedral cells (in thousands) for the 30 %-porosity TPMS, along with the volume averaged velocity magnitude for the simulation at $\boldsymbol{Re_{Dh}} \sim 100$ and the corresponding computed numerical uncertainty (cm/s).

	Grid 1	Grid 2	Grid 3	Grid 4	$\langle U \rangle_V$ (cm/s)
Gyroid	72	36	20	8.7	2.57±0.04
Diamond	75	31	18	8.7	3.2 ± 0.1
SplitP-1	90	51	28	11	3.77 ± 0.08
SplitP-2	99	54	29	15	3.9 ± 0.2

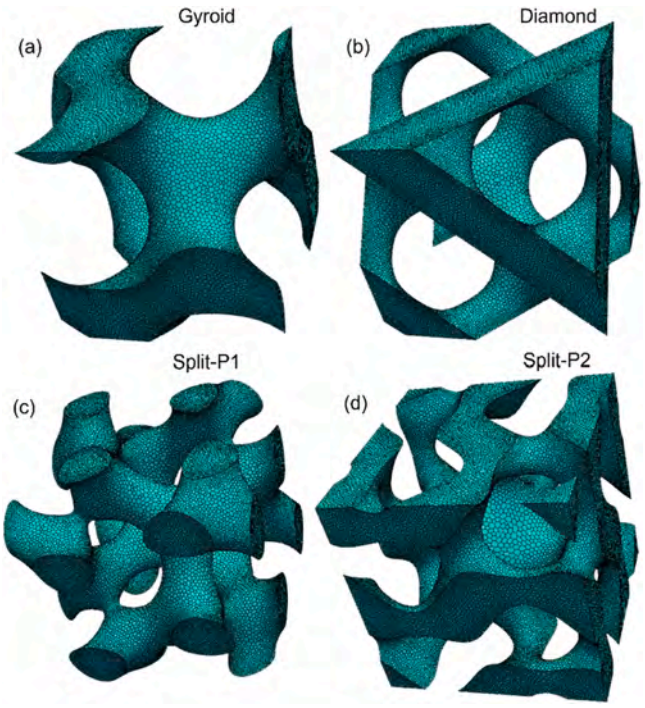

Fig. 4. Surface mesh views: (a) Gyroid, (b) Diamond, (c) Split-P1 and (d) Split-P2.

4.2. Vorticity and flow complexity

Fig. 6 illustrates the normalized vorticity field by its maximum value within the different TPMS at $Re_{Dh} \sim 0.3$ and $Re_{Dh} \sim 100$. At the lower Reynolds number, the Gyroid, Diamond, and Split-P1 show highly organized flow fields, where the vorticity patterns appear regular and stable, reflecting the dominant effect of viscous forces. The Split-P2, on the other hand, already displays more irregular and intricate patterns at the same low Reynolds number, indicating that its geometry tends to induce a more complex flow even under viscous-dominated conditions. As the Reynolds number increases to around 100, all structures exhibit a noticeable increase in flow complexity: the vorticity patterns show greater structural complexity and variability, with intensified swirling and the formation of more irregular flow features throughout the domain. This transition clearly shows the growing influence of inertia on the flow behavior. Notably, the Split-P configurations generate stronger variations in the flow field compared to the Gyroid and Diamond, underlining their greater potential for enhancing internal mixing.

It is important to note that while the vorticity fields are normalized by their maximum values at each Reynolds number, the maximum dimensional vorticity at $Re_{Dh} \sim 100$ is approximately 1000 times higher than at $Re_{Dh} \sim 0.3$. This reflects the substantial increase in rotational motion intensity in the inertial regime, which is visually captured in the LIC patterns as regions of high vorticity become more pronounced and complex.

4.3. Helicity angle and flow alignment

In order to better assess the swirl at different Reynolds numbers, the helicity angle θ is evaluated, as defined in Eq. (10), where $\boldsymbol{\Omega}$ is the vorticity vector, i.e. the rotor of the velocity vector.

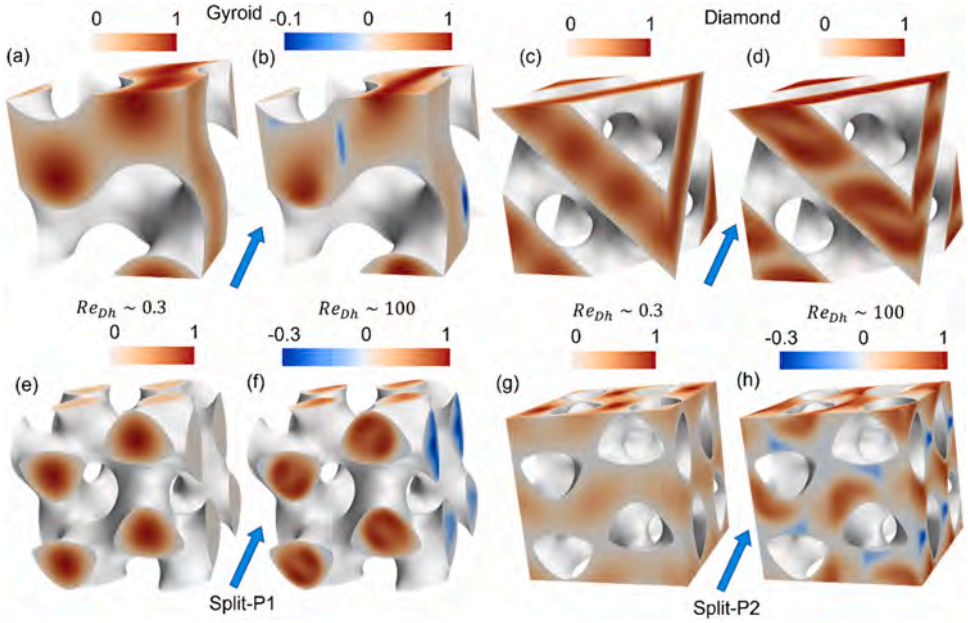

Fig. 5. Normalized velocity in the flow direction for 50 % porosity. (a), (c), (e), (g) $Re_{Dh} \sim 0.3$, (b), (d), (f), (h) $Re_{Dh} \sim 100$ for Gyroid (a),(b), Diamond (c),(d), Split-P1 (e),(f) and Split-P2 (g),(h), respectively.

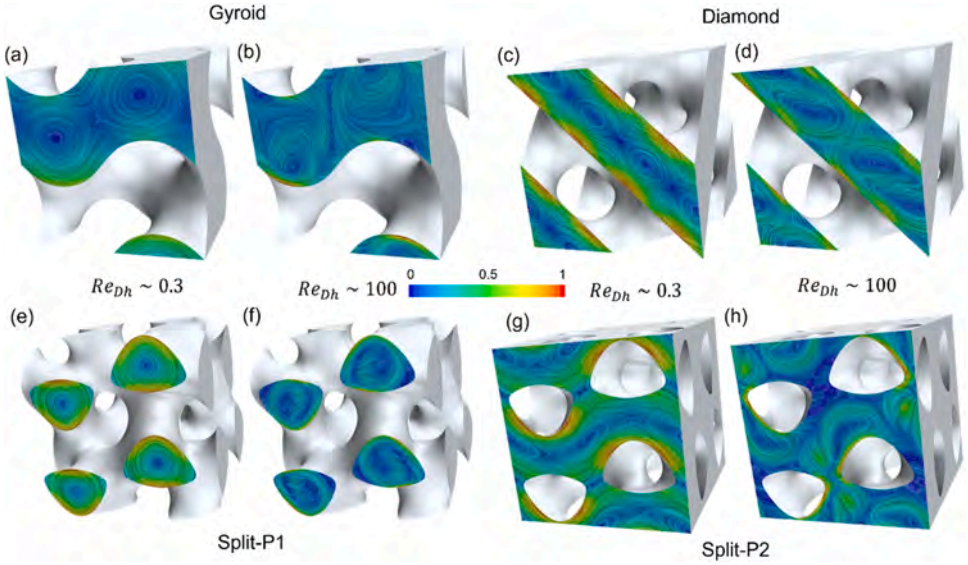

Fig. 6. Line integral convolution of the normalized vorticity within the 50 % porosity TPMS. (a), (c), (e), (g) $Re_{Dh} \sim 0.3$, (b), (d), (f), (h) $Re_{Dh} \sim 100$ for Gyroid (a), (b), Diamond (c),(d), Split-P1 (e),(f) and Split-P2 (g),(h), respectively.

$$\theta = \operatorname{acos}\left(\frac{\boldsymbol{\Omega}\cdot\boldsymbol{u}}{|\boldsymbol{\Omega}|\ |\boldsymbol{u}|}\right) \tag{10}$$

Fig. 7 shows the probability density function (PDF) of the helicity angle in the fluid domain for the different TPMS at $Re_{Dh} \sim 0.3$ (blue bars) and $Re_{Dh} \sim 100$ (orange bars). The helicity angle quantifies the alignment between the velocity and vorticity vectors within the flow, offering insight into local flow structures that affect mixing efficiency and flow stability. A helicity angle of 90° indicates that the vorticity vector is orthogonal to the local velocity direction, characteristic of rotational flow structures such as vortex tubes oriented perpendicular to the main flow. In contrast, angles near 0° or 180° reflect alignment between velocity and vorticity, corresponding to helicoidal (corkscrew-like) motion where fluid particles follow helical paths along the main flow axis [42]. These aligned structures typically promote flow stability and coherence, helping to maintain organized, layered flow and limiting transverse mixing.

Across all TPMS geometries, the PDFs peak near 90°, indicating that the flow predominantly exhibits rotational structures with vorticity oriented transversely to the velocity. This suggests a general tendency toward vortex-dominated flow, which can enhance cross-sectional mixing by inducing rotational motion. At $Re_{Dh} \sim 0.3$, the distributions are sharply peaked around 90°, consistent with a laminar regime dominated by viscous forces, where the flow remains highly organized and stable. Despite the orthogonal alignment, the low inertial forces limit disruption of coherent structures, thus constraining mixing efficiency. At $Re_{Dh} \sim 100$, all TPMS configurations show a broadened helicity angle distribution, reflecting increased flow complexity. The Split-P1 and Split-P2 structures exhibit PDFs similar in shape and width to that of the Diamond configuration, indicating comparable levels of velocity–vorticity misalignment. In contrast, the Gyroid maintains a narrower distribution, suggesting a more organized flow pattern even at higher Reynolds numbers.

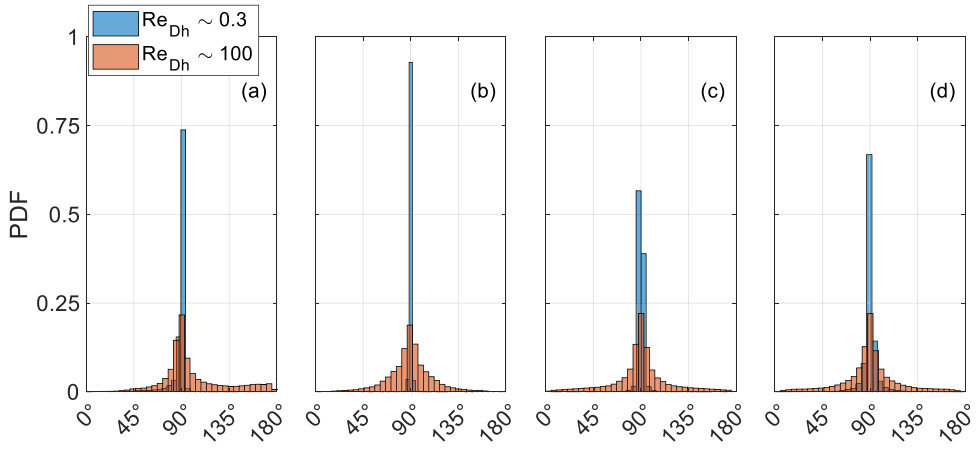

Fig. 7. Probability density function (PDF) of the helicity angle. (a) Gyroid, (b) Diamond, (c) Split-P1 and (d) Split-P2.

4.4. Assessment of the Ergun equation

The Ergun equation [43] is a widely used empirical model for estimating the pressure drop across porous media. It has traditionally proven effective for characterizing flow in porous materials with relatively simple geometries, such as beds of packed spheres, capturing both linear and quadratic dependence on the superficial velocity U_s, thus accounting for both the viscous and the inertial terms, as shown in Eq. (11).

The latter can be rearranged to the dimensionless form of Eq. (12), where Re^* and Δp^* are defined in Eqs. (13) and (14) respectively, and the particle diameter D_p (Eq. (15)) is obtained for sphere packings. Indeed, D_p is considered a good surrogate of an equivalent characteristic length at the scale of the pore.

$$\frac{\Delta p}{L} = 150\left(\frac{\mu U_s}{D_p^2}\right)\frac{(1-\varphi)^2}{\varphi^3} + \frac{7}{4}\left(\frac{\rho U_s^2}{D_p}\right)\left(\frac{1-\varphi}{\varphi^3}\right) \tag{11}$$

$$\Delta p^* = \frac{150}{Re^*} + \frac{7}{4} \tag{12}$$

$$\Delta p^* = \left(\frac{\Delta p}{\rho U_s^2}\right)\left(\frac{D_p}{L}\right)\left(\frac{\varphi^3}{1-\varphi}\right) \tag{13}$$

$$Re^* = \frac{\rho D_p U_s}{\mu(1-\varphi)} \tag{14}$$

$$D_p = \frac{3}{2}\frac{(1-\varphi)}{\varphi}D_h \tag{15}$$

The primary objective of this section is to compare the predicted pressure drop obtained applying the Ergun equation to the complex TPMS geometries investigated here against the numerical results obtained through computational simulations. These TPMS structures significantly differ from the random packings Ergun equation was originally designed for. Thus, it is critical to assess whether the Ergun coefficients and assumptions are still valid, or if significant deviations suggest the need for an alternative or modified approach.

As shown in Fig. 8, across the entire range of Reynolds numbers Re^*, the deviation between CFD results and Ergun equation remains significant, even at $Re^* < 1$, where viscous effects dominate. The error bars indicate that for all TPMS configurations, including simpler geometries like Gyroid and Diamond, the relative error is already above 30–50 % at

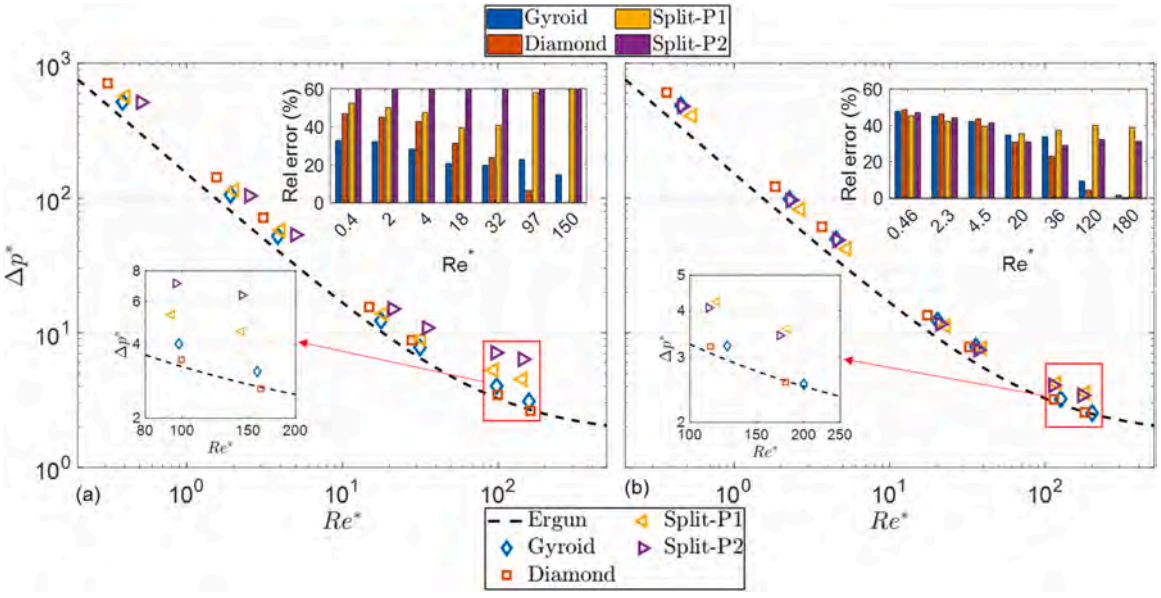

Fig. 8. Comparison of TPMS results with the Ergun equation at different porosities with zooms in the inertial region: (a) 30 % and (b) 60 %. The relative errors for Split-P2 in (a) exceed the maximum value of the axis and are well beyond 100 % for the highest Re^* value.

low Re^*. This discrepancy becomes even more pronounced for more complex structures, such as the two Split-P configurations. While the difference between CFD results and Ergun equation decreases for the Gyroid and Diamond structures at higher porosity and Reynolds numbers, it overall remains unacceptably large, particularly for the Split-P structures. These observations underscore the insufficiency of Ergun equation in accurately modeling pressure drop in intricate TPMS configurations.

Modified versions of the Ergun equations were developed for some of the TPMS analyzed here by other authors. The comparison between CFD results for Gyroid (Fig. 9a) and Diamond (Fig. 9b) structures with the modified versions of Ergun equation by Cheng et al. [29] and Hawken et al. [10] reveals notable differences in predictive accuracy. The correlation of Cheng et al. [29], which was developed for both Gyroid and Diamond, tends to better capture the pressure drop for the Gyroid, in the higher Re^* region, while significant discrepancies are evident at low Re^*. However, for the Diamond structure, the Cheng's model shows significant deviation at higher Reynolds numbers, indicating an increasing mismatch as inertial effects dominate.

For the Diamond structure, the model of Hawken et al. [10], which was specifically developed for this geometry, shows good agreement with the CFD data in the high Re^* range, compared to Cheng's model. However, it still does not fully capture the detailed flow resistance across all Reynolds number ranges, especially at lower Re^*, where viscous effects are significant. These observations imply that neither of the two modifications is fully adequate for accurately modeling pressure drops in complex TPMS structures like Gyroid and Diamond across all flow regimes.

4.5. Assessment of the Darcy and Darcy-Forchheimer relations

The Darcy law (Eq. (16)) models the viscous flow of a fluid through a porous medium for the limit of laminar (low Reynolds) regime, where K is the permeability of the porous medium.

$$\frac{\Delta p}{L} = -\frac{\mu}{K} U_s \tag{16}$$

When the flow enters the transition region to the inertial regime, the Darcy law is no longer able to provide an accurate characterization of the pressure-velocity relationship. The non-linearity must be accounted for by adding a quadratic term in the equation, formulated as the Darcy-Forchheimer law (Eq. (17)), where C_F is the inertial drag factor. Note that Rathore et al. [44], studying the solid-Diamond and Gyroid, utilized a cubic relationship between the linear pressure drop and the mean velocity, but here the well-established quadratic Darcy-Forchheimer law is considered.

$$\frac{\Delta p}{L} = -\frac{\mu}{K} U_s - \frac{\rho C_F}{\sqrt{K}} U_s^2 \tag{17}$$

Fig. 10 presents the relationship between linear pressure drop $\Delta p/L$ and superficial velocity U_s for the analyzed TPMS geometries for porosities of 30 %, 40 %, 50 %, and 60 %. The results refer to a water flow at 20 °C. Across all configurations, a linear correlation between pressure drop and superficial velocity is observed up to $Re_{Dh} \sim 10$, represented by the fourth data point in each plot. This linear regime indicates that Darcy law (represented by the dashed lines) accurately captures the flow resistance in this low-velocity, viscous-dominated range. Importantly, this threshold appears consistent across different TPMS types and porosity levels, establishing a clear boundary where Darcy law remains valid up to $Re_{Dh} \sim 10$.

As the Reynolds number exceeds 10, the relationship between pressure drop and velocity becomes nonlinear. In this regime, the Darcy-Forchheimer law (indicated by the dashed-dotted lines) provides a more accurate representation by incorporating an additional inertial term, allowing for the modeling of the observed quadratic increase in pressure drop with velocity.

To quantify the flow resistance parameters for each TPMS and porosity level, the simulation results at different Reynolds numbers were fitted to both the Darcy and the Darcy-Forchheimer equations. This fitting process enabled the extraction of permeability K_{rel} and inertial drag factor C_F, as summarized in Table 2. These parameters characterize the viscous and inertial contributions to flow resistance for each configuration.

To facilitate the comparison of permeability values across different characteristic lengths, the concept of relative permeability, K_{rel}, is introduced. In this study, K_{rel} is calculated by scaling the dimensional permeability K by the square of the cell size L_C, which is fixed at 10 mm. This approach aligns with methodologies employed by Asbai-Ghoudan et al. [24] and Callens et al. [45], who demonstrated that normalizing permeability in this way enables generalization to different characteristic sizes of the porous medium. Although only a single L_C value is considered in the present work, the use of K_{rel} allows for potential extrapolation to other cell sizes. This normalization is thus a practical step to make the present permeability results more versatile without requiring the analysis of multiple cell sizes for correlation.

The permeability K_{rel} increases with porosity across all TPMS structures, reflecting a reduction in flow resistance within more open configurations. In contrast, the inertial drag factor C_F decreases with porosity, indicating a reduced impact of inertial effects in higher-porosity structures. This trend is consistent across all geometries, with Gyroid and Diamond generally exhibiting higher permeability and lower inertial drag factors compared to the more complex Split-P1 and Split-P2 structures. This difference in behavior highlights the impact of TPMS geometry on flow characteristics, with simpler structures like Gyroid

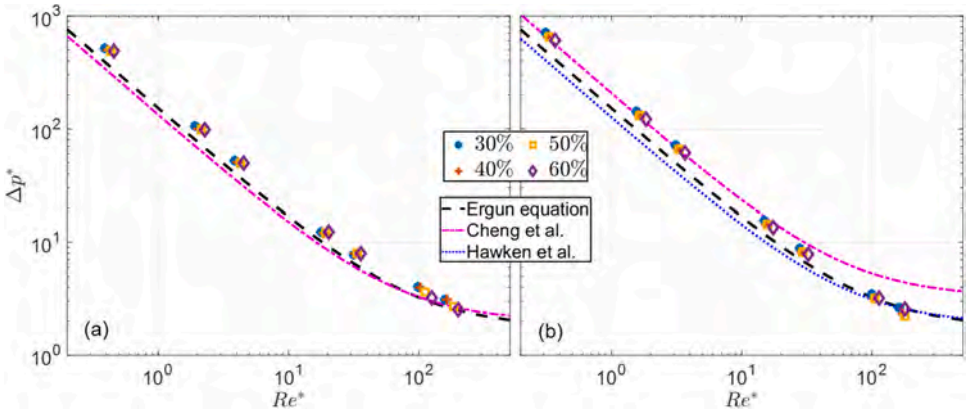

Fig. 9. Comparison of CFD results with modified Ergun equations by Hawken et al. and Cheng et al. (a) Gyroid, (b) Diamond.

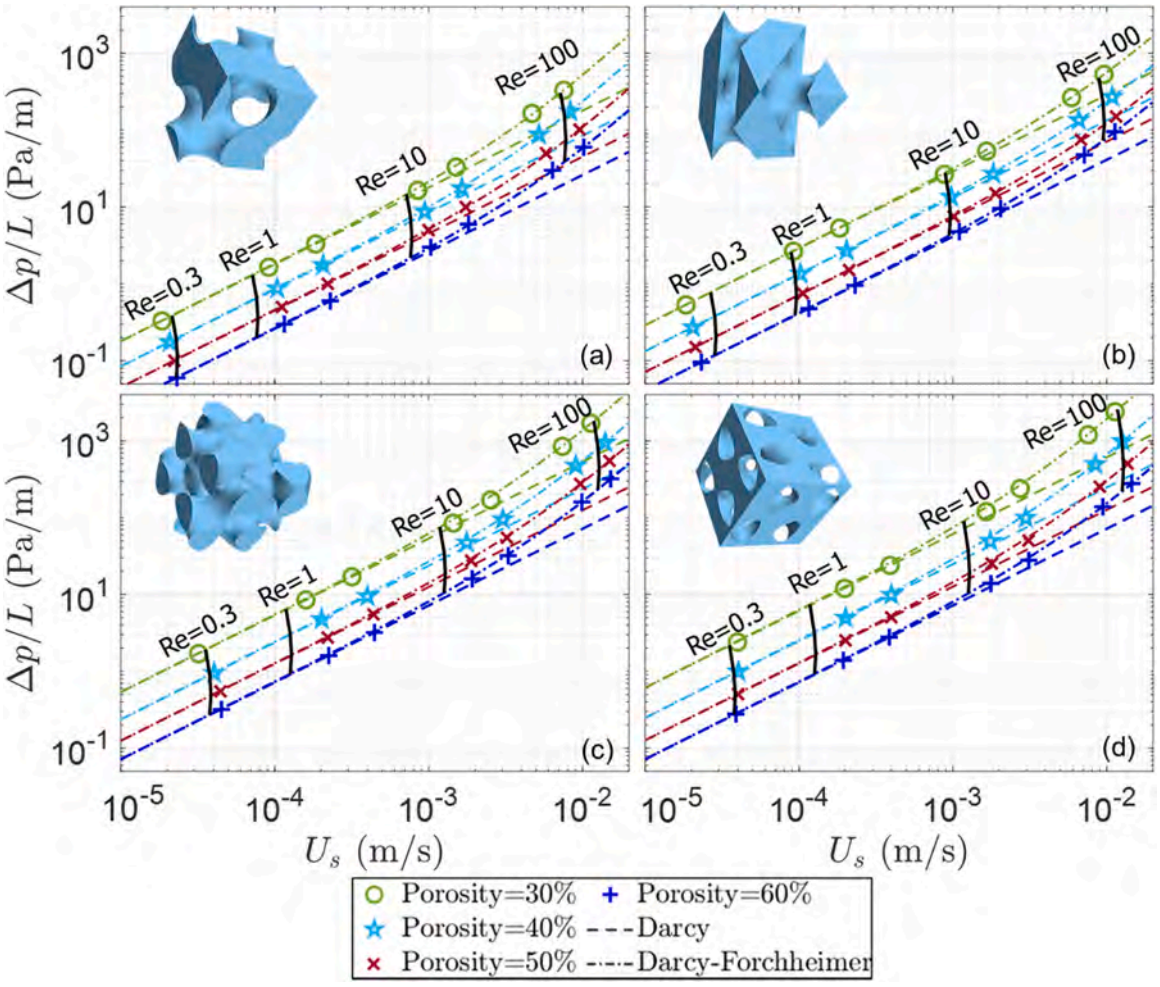

Fig. 10. Linear pressure drop vs superficial velocity for water. (a) Gyroid, (b) Diamond, (c) Split-P1 and (d) Split-P2.

Table 2
Power law fitting parameters (K_{rel} and C_F) for the different TPMS and porosities.

φ (%)	Gyroid		Diamond		Split-P1		Split-P2	
	K_{rel}	C_F	K_{rel}	C_F	K_{rel}	C_F	K_{rel}	C_F
30	5.6e-4	0.81	3.5e-4	0.52	1.9e-4	1.2	1.6e-4	1.7
40	1.2e-3	0.53	7.6e-4	0.30	4.3e-4	0.65	4.1e-4	0.85
50	2.2e-3	0.31	1.4e-3	0.20	8.1e-4	0.46	8.0e-4	0.50
60	3.9e-3	0.20	2.4e-3	0.19	1.4e-3	0.34	1.4e-3	0.31

and Diamond allowing for smoother flow paths and thus lower drag. The high-quality fits achieved in all cases underscore the accuracy of the Darcy-Forchheimer model in describing the flow behavior across the range of TPMS structures and porosity levels analyzed. The results obtained here are not directly compared to others in literature as most of the works published so far employing the Darcy-Forchheimer law focus on sheet lattices (as [25–28]), rather than solid lattices.

4.6. Porosity-dependent scaling of relative permeability and inertial drag factor in TPMS structures

In order to accurately characterize the fluid flow behavior within each TPMS structure, it is essential to establish correlations for both permeability and inertial drag factor as functions of porosity. These parameters are crucial for predicting pressure drop and flow resistance across different flow regimes, from viscous-dominated to inertia-influenced conditions. Given the geometric complexity of TPMS structures and the variability in flow resistance characteristics between different topologies, structure-specific correlations are necessary to ensure precise modeling.

The plots of Fig. 11 show the dependence of K_{rel} (Fig. 11a) and C_F (Fig. 11b) on porosity for each TPMS geometry.

The relationship between K_{rel} and φ, as well as C_F and φ, is fitted with power law equations as defined in Eqs. (18) and (19).

$$K_{rel} = a\varphi^n \tag{18}$$

$$C_F = b\varphi^m \tag{19}$$

Eqs. (18) and 19 with the values listed in Table 3 are valid for $30\% \leq \varphi \leq 60\%$ and $0.3 \leq Re_{D_h} \leq 100$.

Fig. 11 shows a good fit for all TPMS geometries and porosity values, as verified by the star symbols used for quality assessment of the correlation at $\varphi = 55\%$ as later discussed in Section 5.1.

As shown in Table 3, the exponent n spans a narrow range from approximately 2.8 to 3 across all structures, indicating a consistent response of permeability to changes in porosity among the TPMS topologies. Notably, the exponent found for the Gyroid structure (2.78) aligns closely with the value reported by Zhianmanesh et al. [22], who determined an exponent of 2.54 for the same structure, supporting the robustness of our results within the context of existing literature. This consistency in the exponent values suggests a generalizable relationship for K_{rel} across different TPMS types, enhancing the predictive capability of our correlations.

Regarding the inertial drag factor C_F, some variation in the exponent m is observed, especially between the Split-P configurations. While all

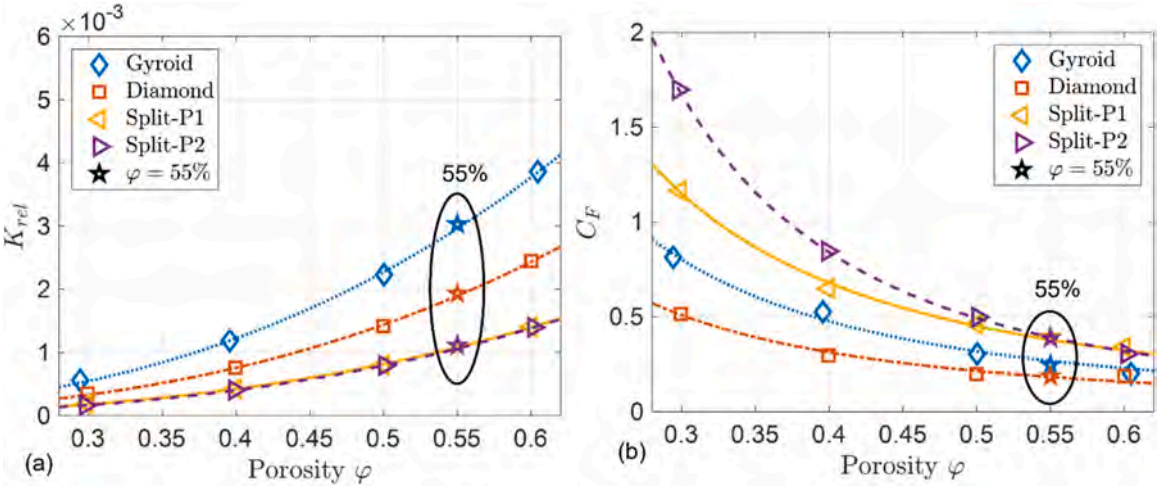

Fig. 11. Relative permeability K_{rel} (a) and inertial drag factor C_F (b) as functions of porosity for the four TPMS topologies, evaluated using Eqs. (18) and 19, respectively. Symbols represent the computed results, lines indicate the corresponding power-law fits, and star symbols denote values used to verify the quality of the developed correlations (see Section 5.1).

Table 3
Power law fitting values for the permeability and inertial factor as a function of the TPMS porosity. The coefficient of determination R^2 of the different fits is also reported.

	TPMS	Gyroid	Diamond	Split-P1	Split-P2
K_{rel}	a	0.0156	0.0106	0.00631	0.00653
	n	2.78	2.89	2.95	3.04
	R^2	0.9994	0.9996	0.9997	0.9999
C_F	b	0.0908	0.0666	0.127	0.0941
	m	−1.81	−1.69	−1.83	−2.39
	R^2	0.9880	0.9788	0.9963	0.9998

TPMS structures show a negative exponent for C_F (indicating a decrease in inertial drag with increasing porosity), the exponent values differ, particularly for Split-P2, which has a larger magnitude of $m = -2.39$ compared to the other structures. This higher sensitivity in Split-P2 reflects its increased drag in the inertial regime, if compared to Split-P1, despite their equal permeability values.

The comparison between the two Split-P structures at 50 % porosity and $Re_{Dh} \sim 100$ reveals insights into why they exhibit the same K_{rel} but different C_F values, as shown in Fig. 11 and Table 3. These differences arise due to the varying nature of the flow field and velocity distribution along the flow direction. Firstly, the normalized cross-sectional area A_c/L_c^2 in Fig. 12a varies along the flow direction for both Split-P1 and Split-P2, reflecting the periodic geometric variations of these structures. However, the average cross-sectional area over the length, $< A_c >_{L_c}$, proportional to the area under the curves, remains the same for both configurations. Indeed, it is proportional to the fluid volume, which is identical for the two structures due to their equal porosity (50 %).

The area under the curves in Fig 12b, proportional to the cross-sectional mean velocity over the cell length, $< \overline{u}_y >_{L_c}$, results to be equal for Split-P1 and Split-P2. Because in the viscous regime, Δp depends on $< A_c >_{L_c}$, the wetted surface area A_{wet}, and $< \overline{u}_y >_{L_c}$ and these parameters are identical for Split-P1 and Split-P2, the pressure drop, described by Darcy's law, is also identical, implying equal permeability values. Differently, in the inertial regime, Δp still depends on $< A_c >_{L_c}$ and A_{wet}, but now on the square of the mean cross sectional velocity over the cell length, $< \overline{u}_y^2 >_{L_c}$. This quantity, proportional to the area under the curves in Fig. 12c, differs between Split-P1 and Split-P2. As a result, when applying the Darcy–Forchheimer law, the inertial drag factor C_F must differ for Split-P1 and Split-P2.

In Fig. 13a, which shows the Gyroid structure, the correlation from Lu et al. [23] (dashed red line) lies within the 95 % confidence interval of the present study correlation across the entire range of porosities. The results from Zhianmanesh et al. [22] and Dolamore et al. [37] also fall largely within the confidence bounds of the present study, indicating a high degree of consistency in the permeability behavior predicted for the Gyroid structure. This alignment across multiple sources strengthens the validity of the present correlation for Gyroid, supporting its predictive

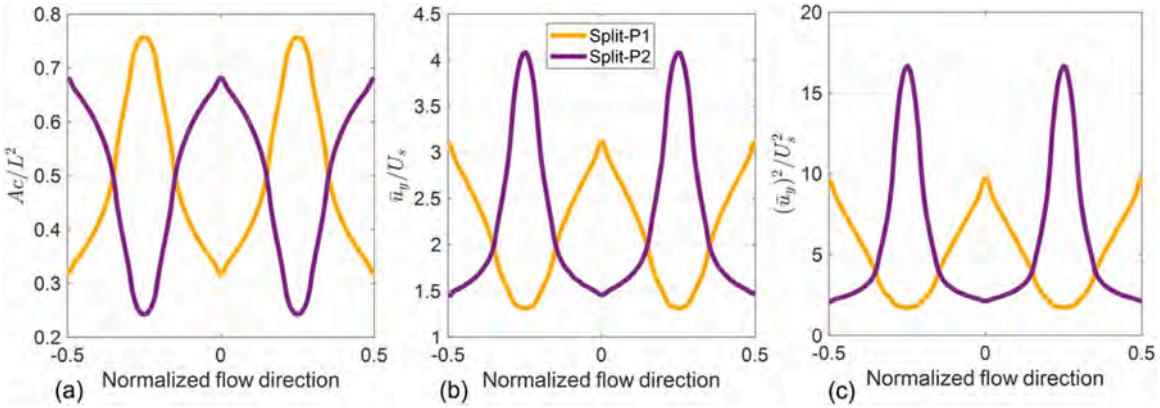

Fig. 12. Comparison between the two Split-P structures at 50 % porosity and $Re_{Dh} \sim 100$: (a) normalized cross sectional area, (b) normalized velocity in the flow direction and (c) square of the normalized velocity in the flow direction.

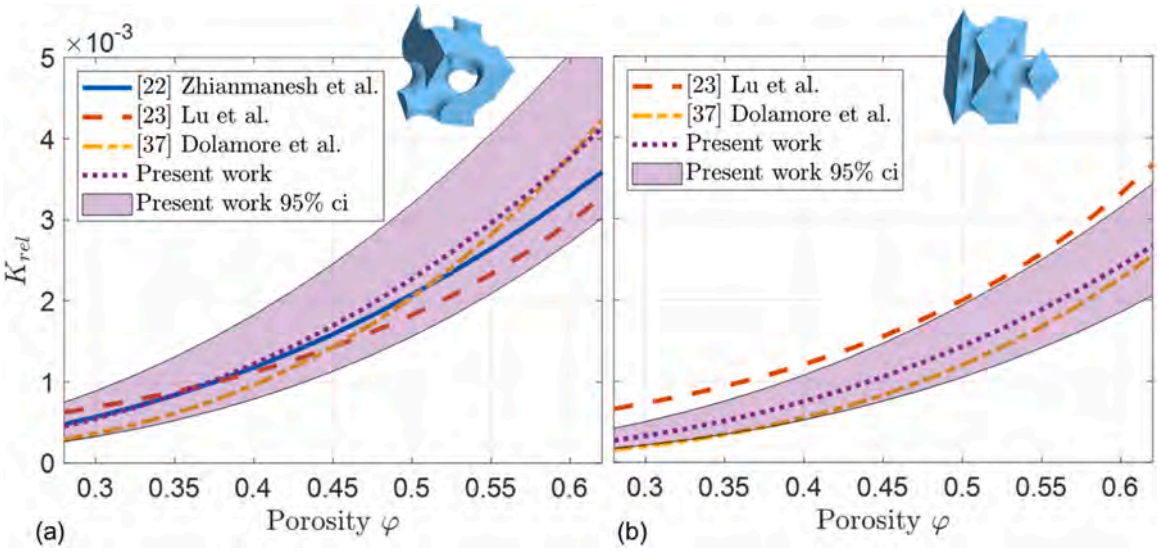

Fig. 13. Comparison in terms of relative permeability between results from literature and present work, and 95 % confidence interval for the present work. a) Gyroid, b) Diamond.

capability across the tested porosity range.

In contrast, Fig. 13b, which displays the Diamond structure, shows a different pattern. Here, the correlation from Lu et al. [23] lies outside the 95 % confidence interval of the present study, especially at higher porosities, predicting higher permeability values. Dolamore et al. [37], however, aligns closely with the present study correlation and remains well within the confidence interval, especially at mid-to-high porosities. This consistency with Dolamore et al. [37] supports the accuracy of the present correlation for the Diamond structure. The 95 % confidence interval for the present study serves as a reliable benchmark, encapsulating most of the permeability trends reported in previous literature for both Gyroid and Diamond structures. The fact that Lu et al. [23] values fall within the confidence interval for Gyroid but outside for Diamond underscores the importance of geometry-specific evaluations and the potential variability introduced by different modeling approaches.

4.7. Application of the Kozeny-Carman equation to permeability-porosity relations in TPMS structures

The Kozeny-Carman equation, in Eq. (20), is a fundamental model to describe the relationship between permeability and porosity in porous media. It models permeability as a function of porosity, the surface-to-volume ratio S_V and the dimensionless Kozeny constant C_K.

$$K_{KC} = C_K \frac{\varphi^3}{S_V^2} \tag{20}$$

Originally developed for packed beds, the Kozeny-Carman equation has been adapted to TPMS structures due to its ability to capture the dependence of permeability on structural parameters, like φ and S_V.

In this study, the Kozeny-Carman approach is further modified by modeling C_K as a quadratic function of porosity (Eq. (21)), as also proposed by Montazerian et al. [21]:

$$C_K = c_0 + c_1 \varphi + c_2 \varphi^2 \tag{21}$$

This quadratic dependence of C_K on φ is expected, given that the square of the surface-to-volume ratio S_V^2 also has a quadratic dependence on porosity (from Eq. (6) and Section 2.3, $\frac{A}{S_V} = 4\varphi \frac{V_{tot}}{A_{wet}}$, where $A_{wet} \sim \varphi^2$), so that the cubic dependence on porosity remains valid for the permeability. This is consistent with the exponents (with a value of approximately 3) derived in Section 4.6 for the permeability of all analyzed TPMS configurations.

Table 4 presents the fitting coefficients c_0, c_1, and c_2 for each TPMS configuration. Eq. (21) with the values listed in Table 4 is valid for $30\% \leq \varphi \leq 60\%$.

Therefore, in agreement with the results of Section4.5, for a given porosity value Gyroid has the highest permeability, followed by Diamond, Split-P1 and Split-P2. In Fig. 14, it can be observed that Gyroid and Diamond have relatively higher C_K values at lower porosities, with Gyroid displaying the highest values among the analyzed TPMS structures. As porosity increases, the C_K values for all structures converge. This is particularly noticeable at porosity values around 0.55 to 0.6, where the C_K values for all structures are nearly identical.

4.8. Permeability-porosity-tortuosity relations

In porous media, permeability K_{rel} and inertial drag factor C_F are influenced by structural parameters such as porosity φ and tortuosity τ. For TPMS structures, these correlations can be described using power law relationships, incorporating both porosity and tortuosity:

$$K_{rel} = a_1 \varphi^k \tau^l \tag{22}$$

$$C_F = a_2 \varphi^p \tau^q \tag{23}$$

The correlations of Eqs. (22) and 23 with the values listed in Table 5 are valid for $30\% \leq \varphi \leq 60\%$ and $0.3 \leq Re_{Dh} \leq 100$. Fig. 15a and b illustrate the dependence of K_{rel} on porosity and tortuosity, respectively, with the exponents listed in Table 5. Across all TPMS structures, K_{rel} increases with porosity and decreases with tortuosity, but the degree of sensitivity varies by geometry. For a given porosity, tortuosity is fixed for each structure. Indeed it is a geometric parameter, as discussed in Section 2.3.

The coefficient k represents the sensitivity of K_{rel} to porosity. The Gyroid has the highest $k = 3.77$, which reflects its relatively open geometry and high sensitivity to porosity changes. The Split-P1 ($k = 3.52$) and Split-P2 ($k = 2.93$) lattices demonstrate a slightly weaker

Table 4
Fitting coefficients for C_K, computed for the different TPMS according to Eq. (21). The value of the R^2 is also reported.

TPMS	Gyroid	Diamond	Split-P1	Split-P2
c_0	6.51	5.52	5.11	4.10
c_1	−20.1	−16.4	−14.7	−11.0
c_2	16.6	13.2	11.7	8.2
R^2	0.9967	0.9977	0.9987	0.9996

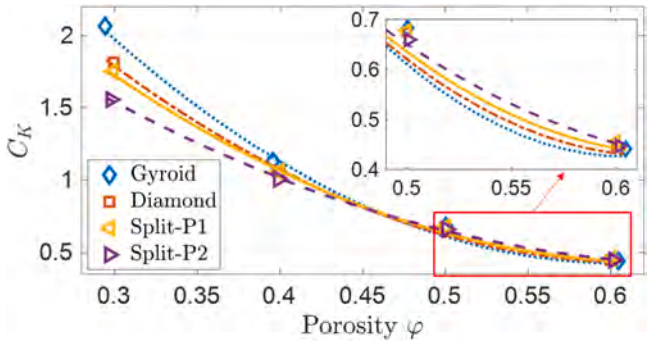

Fig. 14. C_K vs φ for the different TPMS unit cells.

Table 5
Fitting coefficients for the $K_{rel} - \varphi - \tau$ and $C_F - \varphi - \tau$ relations, computed for the different TPMS according to Eqs. (22) and (23), respectively. The value of the R^2 is also reported.

	TPMS	Gyroid	Diamond	Split-P1	Split-P2
K_{rel}	a_1	0.00937	0.0149	0.00624	0.00758
	k	3.77	2.26	3.52	2.93
	l	5.56	−3.08	2.52	−1.81
	R^2	0.9981	1.0000	0.9999	1.0000
C_F	a_2	0.0184	1.27	0.146	0.0514
	p	−0.629	−5.18	−0.0537	−2.18
	q	11.2	−21.3	6.69	6.10
	R^2	0.9991	0.9978	0.9999	0.9998

dependence, indicating that their more tortuous pathways moderate the increase in permeability as porosity rises. The Diamond has the lowest $k = 2.2$, suggesting that permeability in this structure is less influenced by porosity changes compared to the others.

The coefficient l governs the influence of tortuosity on K_{rel}. For Gyroid ($l = 5.56$) and Split-P1 ($l = 2.52$), the positive values indicate that decreases in tortuosity with increasing porosity lead to a more gradual increase in permeability. In contrast, for Diamond ($l = -3.08$) and Split-P2 ($l = -1.81$), the negative l values suggest that decreases in tortuosity significantly amplify any increases in permeability.

Fig. 16a and b illustrate the dependence of C_F on porosity and tortuosity, respectively. These relationships highlight the inverse trend between C_F and porosity, as well as the direct trend between C_F and tortuosity, with variations in sensitivity governed by the p and q exponents (Table 5).

For the Diamond, despite its sharp decrease in C_F with porosity ($p = -5.18$), the large negative tortuosity coefficient ($q = -21.3$) smooths this decline. The combination of these effects results in a more gradual decrease in C_F, as seen in Fig. 16a, where the Diamond exhibits the least pronounced reduction in C_F, compared to other TPMS, at increasing porosity. For the remaining structures the positive q coefficients associated with tortuosity further contribute to the decrease in C_F as porosity increases, reinforcing the trend driven by the p coefficients.

5. Model validation and applicability to TPMS-based systems

The correlations developed in this work for permeability (K_{rel}) and inertial drag factor (C_F), along with the Karman-Cozeny permeability (K_{KC}), offer a comprehensive framework for predicting pressure drop in TPMS structures using the Darcy-Forchheimer equation across both viscous and inertial regimes. However, their validity and applicability must be critically assessed through direct comparisons with high fidelity numerical simulations. In this section, a two-step validation process is performed to evaluate the effectiveness and generalizability of these models.

First, the developed correlations are validated by simulating a single unit cell with a porosity of 55 %, comparing the pressure drop results from numerical simulations with those predicted by the derived permeability-porosity, permeability-porosity-tortuosity, and Kozeny-Carman-based models. Additionally, the widely used Ergun correlation is also included. This comparison serves as a benchmark for assessing the predictive accuracy of the Darcy-Forchheimer equation with the relations developed in this study. Second, the validation is extended to a more practical scenario by simulating a pipe section filled with the different TPMS geometries analyzed in this work. The goal is to evaluate whether the correlations, derived for a single unit cell, can reliably predict the pressure drop in more complex configurations, such as heat sinks or fluid channels filled with multiple TPMS unit cells where the presence of the walls is also considered. By comparing the results from these simulations with predictions based on single-cell models, the feasibility of scaling the developed models to larger, real-world systems is analyzed.

5.1. Discussion of model predictions for the single unit cell domain

Fig. 17 shows the analysis for a single TPMS unit cell with 55 % porosity. Although this porosity value differs from those used to derive the developed correlations, it remains within the porosity range covered by the models, enabling a meaningful validation of their predictive accuracy.

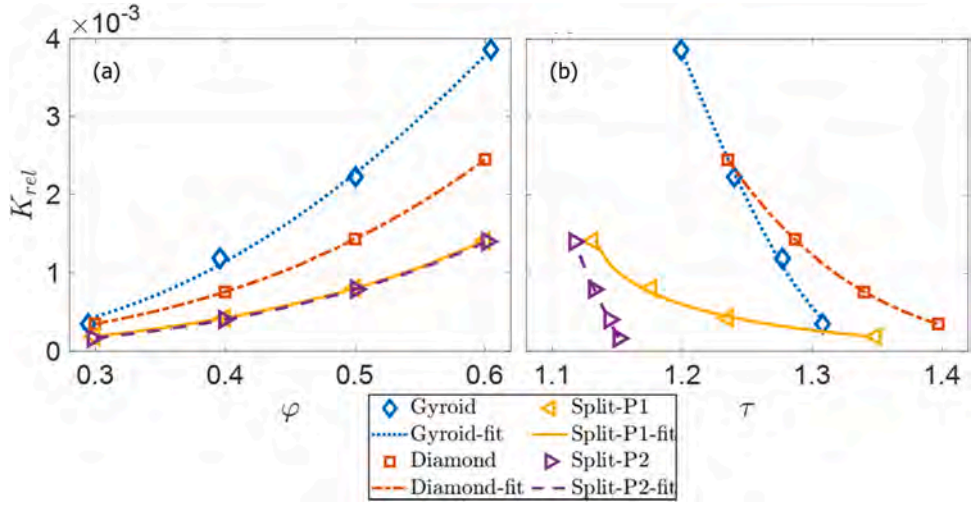

Fig. 15. Relative permeability K_{rel} as a function of porosity (a) and tortuosity (b), according to Eq. (22).

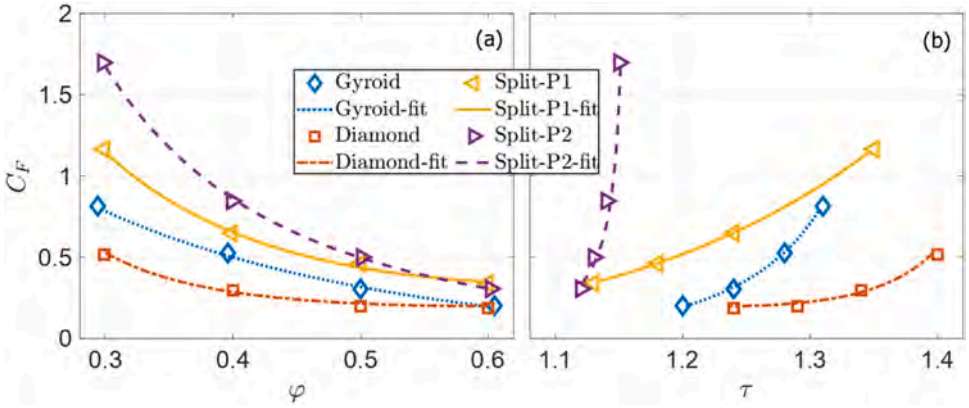

Fig. 16. Inertial drag factor, C_F, as a function of porosity (a) and tortuosity (b), according to Eq. (23).

The relative error is computed as:

$$\textit{Relative error}\ (\%) = \frac{\Delta p_{CFD} - \Delta p_{corr}}{\Delta p_{CFD}} \cdot 100 \tag{24}$$

The Kozeny-Carman relation, designed for permeability prediction in the viscous-dominated regime, is only compared at low Reynolds numbers $Re_{Dh} \sim 5$. It consistently underperforms compared to the developed $K_{rel} - \varphi$ and $K_{rel} - \varphi - \tau$ correlations. Even for simpler geometries such as Gyroid and Diamond, the Kozeny-Carman relation fails to match the accuracy of the developed models, emphasizing its limited applicability to TPMS structures.

The developed models, based on $K_{rel} - \varphi$ and $K_{rel} - \varphi - \tau$ relations, demonstrate strong predictive capabilities across all Reynolds numbers and TPMS geometries. Relative errors are consistently below 10 %, with only minor differences between the two formulations. The similar performance of these models suggests that incorporating the tortuosity τ in addition to porosity φ does not significantly enhance the predictive accuracy. This can be attributed to the interdependence of φ and τ, as discussed in Section 2.3 and shown in Fig. 2d Since τ and φ are not entirely independent variables, the simpler $K_{rel} - \varphi$ model is sufficient for practical use, providing nearly identical results with reduced computational complexity.

The Ergun equation, while widely used for porous media, performs poorly across all Reynolds numbers and TPMS structures. At low Reynolds numbers, it consistently underpredicts pressure drop, with large errors particularly for the Split-P geometries, where the complex flow pathways deviate significantly from the assumptions underlying the Ergun model. Even at higher Reynolds numbers $Re_{Dh} \sim 100$, where inertial effects dominate, the Ergun equation shows only marginally improved accuracy for the Gyroid and Diamond structures but remains unreliable for Split-P geometries. This indicates that the Ergun model lacks the ability to account for the geometric complexity and tortuosity of TPMS.

5.2. Discussion of model predictions for a pipe filled with TPMS

Two pipe geometries with diameters of 20 *mm* and 40 *mm*, both with a total length of 50 mm and filled with TPMS, are simulated. The unit cells size is $L_C = 5$ *mm*, smaller than the 10 *mm* unit cell size used in the development of the correlations. This design choice enables testing the scalability of the developed K_{rel} correlations to L_C different from those used during their formulation. Fig. 18 exemplarily illustrates the 40 mm diameter pipe filled with the four different TPMS structures, all configured at a porosity of 60 %. Periodic boundary conditions with a specified pressure drop were applied at the inlet and outlet of the pipe to minimize the computational domain and reduce computational expense, while the internal surface and the external walls were set as no-slip. The same discretization schemes and solution algorithm used for the single unit cell and described in Section3.2 are also adopted here. The grid generation strategy, optimized for accuracy and computational efficiency in single cells simulations, is consistently applied to larger geometries to ensure consistency across scales. This approach results in a highly detailed grid and computationally intensive simulations. For example, for the larger 40 *mm* pipe, this methodology leads to a substantial number of computational cells, which is representative of the high computational cost associated with simulating real heat sinks filled with TPMS structures. These high computational costs underscore the practical importance of developing reliable permeability and inertial drag factor correlations to reduce dependency on full-scale CFD simulations during the design and optimization of such equipment.

The predicted pressure drops for a water flow at 20 °C were compared to CFD simulations under two flow regimes ($Re_{Dh} \sim 5$ and

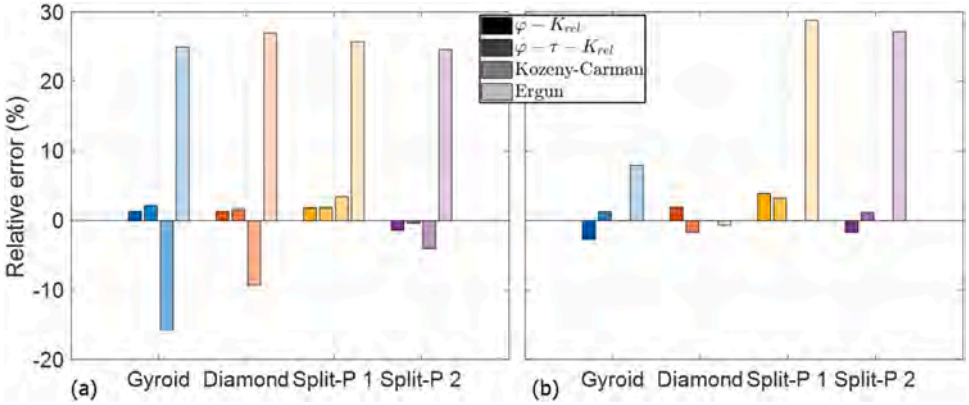

Fig. 17. Comparison of predicted pressure drop for the unit cell with 55 % porosity using the developed models and CFD results. (a) $Re_{Dh} \sim 5$, (b) $Re_{Dh} \sim 100$.

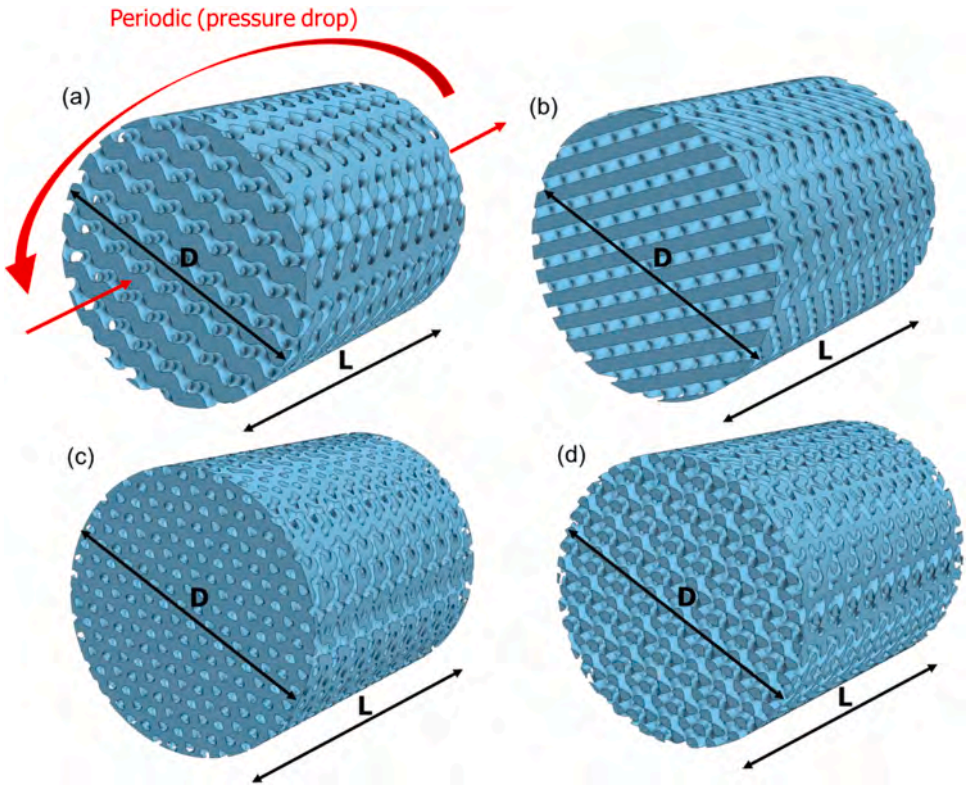

Fig. 18. Geometry and boundary conditions of the pipes $D = 40$ mm diameter (and $L = 50$ mm). a) Gyroid, b) Diamond, c) Split-P1 and d) Split-P2.

$Re_{Dh} \sim 100$). Figs. 19 and 20 provide an overview of these comparisons, highlighting the relative errors and model performance under varying conditions.

The developed $K_{rel} - \varphi$ and $K_{rel} - \varphi - \tau$ correlations demonstrated superior accuracy compared to the Ergun and Kozeny-Carman equations. The relative errors for the developed models were consistently <10 % across all configurations and Reynolds numbers, with the exception of Split-P1, where the error reached a maximum of 21 %. In contrast, the Ergun equation produced errors as high as 30 %, particularly for Split-P geometries. This highlights the inability of the Ergun equation to capture the nuanced flow behavior within the complex geometries of TPMS structures. In the low Reynolds number regime ($Re_{Dh} \sim 5$), the Kozeny-Carman relation performed similar or worse than the developed correlations.

Also here a notable agreement exists between predictions made using $K_{rel} - \varphi$ and $K_{rel} - \varphi - \tau$ correlations, for the same reasons discussed in Section 5.1 for the single unit cell. Consequently, the simpler $K_{rel} - \varphi$ correlation is recommended for practical applications due to its comparable accuracy and lower computational complexity.

The differences in pressure drop results between the pipe geometries and the single unit cell can be partially explained by the variation in hydraulic diameter D_h. In the pipes, the presence of the external wall modifies the wetted area A_{wet} compared to the single cell configuration, resulting in deviations in D_h. These differences are more pronounced for

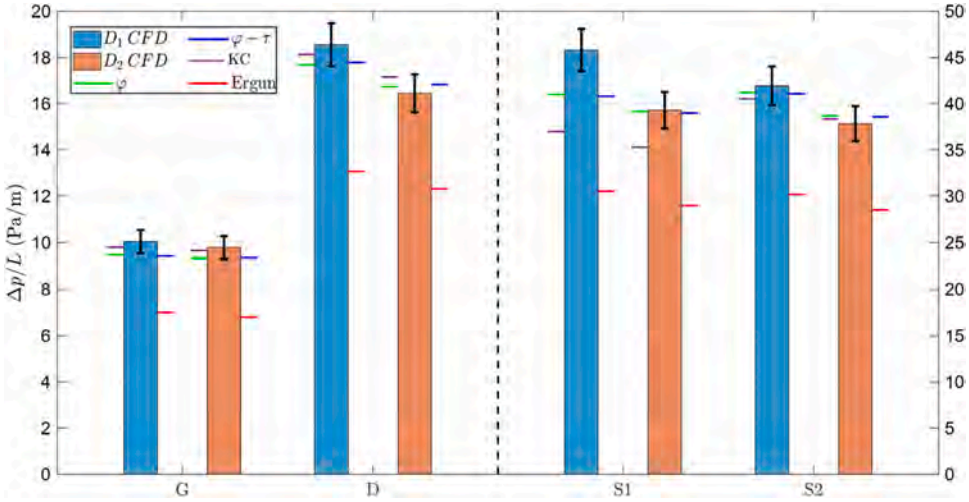

Fig. 19. Comparison of predicted linear pressure drops of water in the pipes at $Re_{Dh} \sim 5$, using the developed models and CFD results. φ and $\varphi - \tau$ in the legend refer to the developed power laws for the permeability, one depending only on porosity, and the other on porosity and tortuosity. *KC* refers to the Kozeny-Carman equation. The horizontal lines refer to the models predictions.

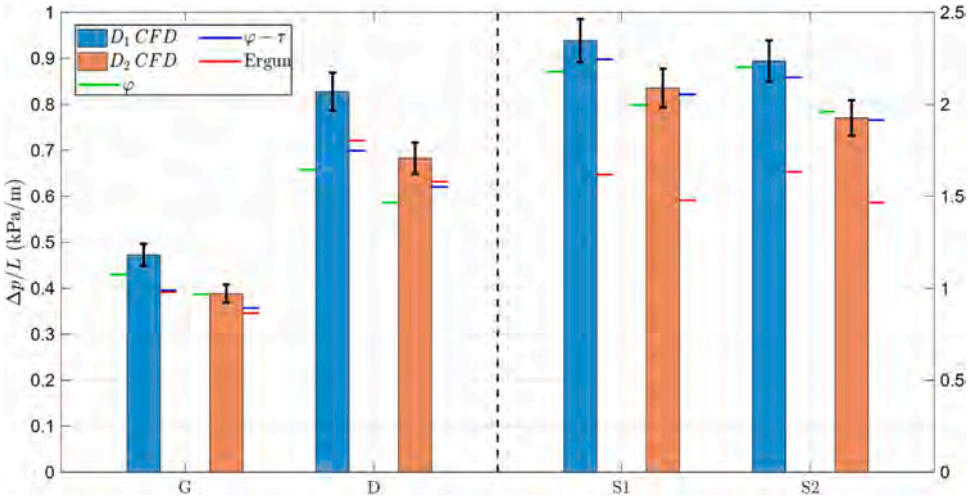

Fig. 20. Comparison of predicted linear pressure drops of water in the pipes at $Re_{Dh} \sim 100$, using the developed models and CFD results. φ and $\varphi - \tau$ in the legend refer to the developed power laws for the inertial drag factors, one depending only on porosity, and the other on porosity and tortuosity. The horizontal lines refer to the models predictions.

simpler geometries like Gyroid or Diamond, where the wall significantly alters A_{wet}, while more complex geometries exhibit less sensitivity to the wall effects. The smaller D_h in the pipe configurations, at the same Re_{Dh} , leads to a higher superficial velocity and, consequently, a higher linear pressure drop. This effect is particularly noticeable in the smaller diameter pipe $D_1 = 20$ *mm*, where the reduced D_h amplifies the velocity and thus pressure drop compared to the larger diameter pipe $D_2 = 40$ *mm*. Despite these geometric differences, the model predictions are mostly within the uncertainty of the CFD results for both pipe sizes. This robustness highlights the scalability of the developed correlations to configurations beyond single unit cells, demonstrating their potential for use in practical engineering applications. The relatively small influence of pipe diameter on the predictive performance further emphasizes the generalizability of the models.

6. Summary and conclusions

This study presents a comprehensive investigation into the hydrodynamic behavior of solid-type TPMS, with a focus on the Gyroid, Diamond, and Split-P geometries. Flow characteristics were analyzed using CFD simulations across a wide range of Reynolds numbers ($0.3 \leq Re_{Dh} \leq 100$), spanning from viscous to weakly inertial regimes, and porosities between 30 % and 60 %. One single TPMS cell with periodic boundary conditions was investigated, representing a reference element volumae of an infinite lattice. Two modeling frameworks were employed for pressure drop prediction: the Ergun equation and the Darcy-Forchheimer equation, the latter enhanced with newly developed correlations for permeability and inertial drag factor. Additionally, an adapted Kozeny-Carman equation was introduced to extend its applicability to TPMS geometries for permeability prediction. The permeability and inertial drag factor correlations were expressed as power-law functions of porosity and tortuosity. While the inclusion of tortuosity provided an additional predictive layer, it was found that due to the intrinsic relationship between porosity and tortuosity, porosity-based correlations alone produced similar accuracy. The proposed models demonstrated strong agreement with CFD results, achieving relative errors below 10 % for most configurations and a maximum error of 21 % for the more complex Split-P1 geometry. This performance significantly surpassed that of the Ergun equation, which exhibited errors as high as 30 % for the Split-P configurations. Validation in larger-scale geometries, such as pipes filled with TPMS, confirmed the scalability and robustness of the developed correlations. Despite variations in hydraulic diameter caused by wall effects, the proposed models accurately predicted pressure drops in these configurations. This underscores their reliability for practical applications, including heat sinks and porous media systems.

In conclusion, this work provides a robust framework for modeling flow in TPMS geometries, enhancing their potential for engineered porous media applications in fluid transport and thermal management systems. By reducing reliance on computationally expensive CFD simulations, these correlations offer a practical tool for the design and optimization of TPMS-based systems. Future research should aim to integrate thermal effects, investigate additional TPMS topologies, and explore configurations with nonuniform porosities to broaden the applicability and utility of these findings.

CRediT authorship contribution statement

E. Gajetti: Writing – review & editing, Validation, Writing – original draft, Software. **G. Boccardo:** Writing – review & editing, Supervision. **L. Savoldi:** Writing – review & editing, Supervision, Resources, Project administration, Methodology, Formal analysis, Conceptualization. **L. Marocco:** Methodology, Formal analysis, Conceptualization, Writing – review & editing, Supervision.

Declaration of competing interest

The authors declare that they have no known competing financial interests or personal relationships that could have appeared to influence the work reported in this paper.

Acknowledgements

The authors acknowledge the use of computational resources provided by hpc@polito, which is a project of Academic Computing within the Department of Control and Computer Engineering at the Politecnico di Torino (http://www.hpc.polito.it).

This research was funded by CETPartnership, the Clean Energy Transition Partnership under the 2023 joint call for research proposals, co-funded by the European Commision (GA N°101069750) and with the funding organizations detailed on https://cetpartnership.eu/funding-agencies-and-call-modules.

We are also grateful to Prof. A. Buffo for the helpful discussions.

Data availability

Data will be made available on request.

References

[1] Bestimmung zweier speziellen periodischen Minimalflächen, auf welchen unendlich viele gerade Linien und unendlich viele ebene geodätische Linien liegen. Frenckell. Accessed: Sep. 16, 2024. [Online]. Available: http://resolver.sub.uni-goettingen.de/purl?PPN591417707.

[2] N. Baobaid, M.I. Ali, K.A. Khan, R.K. Abu Al-Rub, Fluid flow and heat transfer of porous TPMS architected heat sinks in free convection environment, Case Stud. Thermal Eng. 33 (May 2022), https://doi.org/10.1016/J.CSITE.2022.101944.

[3] F. Salmon, D. Lacanette, M. Duquesne, A. Godin, 3D fluid–structure simulation of innovative composites for the design and thermal management of electronic devices, Energy Convers. Manage 280 (Mar. 2023), https://doi.org/10.1016/J.ENCONMAN.2023.116824.

[4] D. Liang, C. Shi, W. Li, W. Chen, M.K. Chyu, Design, flow characteristics and performance evaluation of bioinspired heat exchangers based on triply periodic minimal surfaces, Int. J. Heat. Mass Transf. 201 (Feb. 2023) 123620, https://doi.org/10.1016/J.IJHEATMASSTRANSFER.2022.123620.

[5] B.W. Reynolds, C.J. Fee, K.R. Morison, D.J. Holland, Characterisation of heat transfer within 3D printed TPMS heat exchangers, Int. J. Heat. Mass Transf. 212 (Sep. 2023) 124264, https://doi.org/10.1016/J.IJHEATMASSTRANSFER.2023.124264.

[6] T. Dixit, E. Al-Hajri, M.C. Paul, P. Nithiarasu, S. Kumar, High performance, microarchitected, compact heat exchanger enabled by 3D printing, Appl. Therm. Eng. 210 (Jun. 2022), https://doi.org/10.1016/J.APPLTHERMALENG.2022.118339.

[7] Z.A. Qureshi, S.A.B. Al-Omari, E. Elnajjar, O. Al-Ketan, R. Abu Al-Rub, Nature-inspired triply periodic minimal surface-based structures in sheet and solid configurations for performance enhancement of a low-thermal-conductivity phase-change material for latent-heat thermal-energy-storage applications, Int. J. Thermal Sci. 173 (Mar. 2022), https://doi.org/10.1016/J.IJTHERMALSCI.2021.107361.

[8] B. Li, Q. Li, G. Zhang, X. Liu, F. Zhong, Z. Yu, Pore-scale numerical simulations on the lean concentration methane combustion in porous medium with gyroid triply periodic minimal surfaces structures, Combus. Sci. Technol. (Mar. 2023), https://doi.org/10.1080/00102202.2023.2194020.

[9] M. Asif, C.A. Grande, TPMS contactors designed with imprinted porosity: numerical evaluation of momentum and energy transport, Ind. Eng. Chem. Res. 61 (50) (Dec. 2022) 18556–18566, https://doi.org/10.1021/ACS.IECR.2C03384/ASSET/IMAGES/LARGE/IE2C03384_0009.JPEG.

[10] M.B. Hawken, S. Reid, D.A. Clarke, M. Watson, C.J. Fee, D.J. Holland, Characterization of pressure drop through Schwarz-Diamond triply periodic minimal surface porous media, Chem. Eng. Sci. 280 (Oct. 2023) 119039, https://doi.org/10.1016/J.CES.2023.119039.

[11] D.A. Clarke, F. Dolamore, C.J. Fee, P. Galvosas, D.J. Holland, Investigation of flow through triply periodic minimal surface-structured porous media using MRI and CFD, Chem. Eng. Sci. 231 (Feb. 2021) 116264, https://doi.org/10.1016/J.CES.2020.116264.

[12] Y. Jung, S. Torquato, Fluid permeabilities of triply periodic minimal surfaces, Phys. Rev. e Stat. Nonlin. Soft. Matter. Phys. 72 (5) (Nov. 2005) 056319, https://doi.org/10.1103/PHYSREVE.72.056319/FIGURES/9/MEDIUM.

[13] D. Ali, M. Ozalp, S.B.G. Blanquer, S. Onel, Permeability and fluid flow-induced wall shear stress in bone scaffolds with TPMS and lattice architectures: a CFD analysis, Eur. J. Mech. - B/Fluids 79 (Jan. 2020) 376–385, https://doi.org/10.1016/J.EUROMECHFLU.2019.09.015.

[14] R. Guerreiro, T. Pires, J.M. Guedes, P.R. Fernandes, A.P.G. Castro, On the tortuosity of TPMS scaffolds for tissue engineering, Symmetry (Basel) 12 (4) (Apr. 2020) 596, https://doi.org/10.3390/SYM12040596, 2020, Vol. 12, Page 596.

[15] D. Karaman, H. Ghahramanzadeh Asl, The effects of sheet and network solid structures of similar TPMS scaffold architectures on permeability, wall shear stress, and velocity: a CFD analysis, Med. Eng. Phys. 118 (Aug. 2023), https://doi.org/10.1016/j.medengphy.2023.104024.

[16] G. Chouhan, B.M. Gunji, Additive manufacturing TPMS lattice structures: experimental study on airflow resistivity, Results Mater. 20 (Dec. 2023) 100478, https://doi.org/10.1016/J.RINMA.2023.100478.

[17] A. Zimmer, J.D. Pacheco Araújo, K.A. Andreassen, C.A. Grande, Effect of manufacturing techniques in pressure drop on triple periodical minimal surface packings, Chem. Ing. Tech. 93 (6) (Jun. 2021) 967–973, https://doi.org/10.1002/CITE.202000237;WGROUP:STRING:PUBLICATION.

[18] J.K. Guest, J.H. Prévost, Design of maximum permeability material structures, Comput. Methods Appl. Mech. Eng. 196 (4–6) (Jan. 2007) 1006–1017, https://doi.org/10.1016/J.CMA.2006.08.006.

[19] D. Liang, K. Yang, H. Gu, W. Chen, M.K. Chyu, The effect of unit size on the flow and heat transfer performance of the 'Schwartz-D' heat exchanger, Int. J. Heat. Mass Transf. 214 (Nov. 2023) 124367, https://doi.org/10.1016/J.IJHEATMASSTRANSFER.2023.124367.

[20] K. Zhang, J.P. Hickey, M. Vlasea, An analysis framework of additively manufactured deterministic porous structures for transpiration cooling, J. Mater. Eng. Perform. 32 (20) (Oct. 2023) 9253–9262, https://doi.org/10.1007/S11665-023-08481-5/FIGURES/11.

[21] H. Montazerian, M. Zhianmanesh, E. Davoodi, A.S. Milani, M. Hoorfar, Longitudinal and radial permeability analysis of additively manufactured porous scaffolds: effect of pore shape and porosity, Mater. Des. 122 (May 2017) 146–156, https://doi.org/10.1016/J.MATDES.2017.03.006.

[22] M. Zhianmanesh, M. Varmazyar, H. Montazerian, Fluid permeability of graded porosity scaffolds architectured with minimal surfaces, ACS. Biomater. Sci. Eng. 5 (3) (Mar. 2019) 1228–1237, https://doi.org/10.1021/ACSBIOMATERIALS.8B01400.

[23] Y. Lu, L.L. Cheng, Z. Yang, J. Li, H. Zhu, Relationship between the morphological, mechanical and permeability properties of porous bone scaffolds and the underlying microstructure, PLoS. One 15 (9) (Sep. 2020) e0238471, https://doi.org/10.1371/JOURNAL.PONE.0238471.

[24] R. Asbai-Ghoudan, S. Ruiz de Galarreta, N. Rodriguez-Florez, Analytical model for the prediction of permeability of triply periodic minimal surfaces, J. Mech. Behav. Biomed. Mater. 124 (Dec. 2021), https://doi.org/10.1016/J.JMBBM.2021.104804.

[25] A.P.G. Castro, T. Pires, J.E. Santos, B.P. Gouveia, P.R. Fernandes, Permeability versus design in TPMS scaffolds, Materials (Basel) 12 (8) (Apr. 2019) 1313, https://doi.org/10.3390/MA12081313, 2019, Vol. 12, Page 1313.

[26] S. Tupin, M. Ohta, Assessing porous Media permeability in non-darcy flow: a re-evaluation based on the Forchheimer equation, Materials (Basel) 13 (11) (Jun. 2020) 2535, https://doi.org/10.3390/MA13112535, 2020, Vol. 13, Page 2535.

[27] V. Novozhilov, et al., Prediction of flow properties of porous triply periodic minimal surface (TPMS) structures, Fluids 8 (12) (Nov. 2023) 312, https://doi.org/10.3390/FLUIDS8120312, 2023, Vol. 8, Page 312.

[28] E.N. Ahmed, A. Bottaro, E.N. Ahmed, A. Bottaro, Flow through porous metamaterials formed by TPMS-based unit cells: effects of advection, EuJMB 100 (Jul. 2023) 202–207, https://doi.org/10.1016/J.EUROMECHFLU.2023.04.002.

[29] Z. Cheng, et al., Investigations on porous media customized by triply periodic minimal surface: heat transfer correlations and strength performance, ICHMT 129 (Dec. 2021) 105713, https://doi.org/10.1016/J.ICHEATMASSTRANSFER.2021.105713.

[30] "Next-gen Engineering Design software: nTop (formerly nTopology) | nTop." accessed: aug. 11, 2023. [Online]. Available: https://www.ntop.com/.

[31] H. Montazerian, et al., Permeability and mechanical properties of gradient porous PDMS scaffolds fabricated by 3D-printed sacrificial templates designed with minimal surfaces, Acta Biomater. 96 (Sep. 2019) 149–160, https://doi.org/10.1016/J.ACTBIO.2019.06.040.

[32] J.W. Fisher, S.W. Miller, J. Bartolai, T.W. Simpson, M.A. Yukish, Catalog of triply periodic minimal surfaces, equation-based lattice structures, and their homogenized property data, Data Brief. 49 (Aug. 2023), https://doi.org/10.1016/J.DIB.2023.109311.

[33] M. Matyka, Z. Koza, How to calculate tortuosity easily? AIP. Conf. Proc. 1453 (1) (Mar. 2011) 17–22, https://doi.org/10.1063/1.4711147.

[34] K.M. Graczyk, M. Matyka, Predicting porosity, permeability, and tortuosity of porous media from images by deep learning, Sci. Rep. 10 (1) (Dec. 2020), https://doi.org/10.1038/S41598-020-78415-X.

[35] J.W. Luo, L. Chen, T. Min, F. Shan, Q. Kang, W.Q. Tao, Macroscopic transport properties of Gyroid structures based on pore-scale studies: permeability, diffusivity and thermal conductivity, Int. J. Heat. Mass Transf. 146 (Jan. 2020) 118837, https://doi.org/10.1016/J.IJHEATMASSTRANSFER.2019.118837.

[36] M. Sauermoser-Yri, et al., On the porosity-dependent permeability and conductivity of triply periodic minimal surface based porous media, J. Mater. Res. Technol. 27 (Nov. 2023) 585–599, https://doi.org/10.1016/J.JMRT.2023.09.242.

[37] F. Dolamore, B. Houlton, C.J. Fee, M.J. Watson, D.J. Holland, A numerical investigation of the hydrodynamic dispersion in triply periodic chromatographic stationary phases, J. Chromatogr. A 1685 (Dec. 2022) 463637, https://doi.org/10.1016/J.CHROMA.2022.463637.

[38] M.G. Gado, et al., Adsorbent beds packed in triply periodic minimal surface-derived structures and their performance in adsorption desalination/cooling systems, ICHMT 150 (Jan. 2024) 107205, https://doi.org/10.1016/J.ICHEATMASSTRANSFER.2023.107205.

[39] T. Pires, J. Santos, R.B. Ruben, B.P. Gouveia, A.P.G. Castro, P.R. Fernandes, Numerical-experimental analysis of the permeability-porosity relationship in triply periodic minimal surfaces scaffolds, J. Biomech. 117 (Mar. 2021), https://doi.org/10.1016/J.JBIOMECH.2021.110263.

[40] A. Gonçalves Pereira Passos, J. Manuel da Silva Chaves Ribeiro Pereira Miguel Abreu de Almeida Mendes, C. Frederico Neves Bettencourt da Silva, and M. Abreu de Almeida Mendes, "Laminar flow and heat transfer in triply periodic minimal surfaces," 2019. Accessed: May 06, 2025. [Online]. Available: https://fenix.tecnico.ulisboa.pt/downloadFile/1126295043836646/ThesisAndrePassos.pdf.

[41] "ASME V&V 20-2009 standard for verification and validation in computational fluid dynamics and heat transfer" (V&V20 Committee Chair).

[42] E. Crevacore, T. Tosco, R. Sethi, G. Boccardo, D.L. Marchisio, Recirculation zones induce non-Fickian transport in three-dimensional periodic porous media, Phys. Rev. e 94 (5) (Nov. 2016) 053118, https://doi.org/10.1103/PHYSREVE.94.053118/FIGURES/8/MEDIUM.

[43] R.Byron Bird, Warren E. Stewart, Edwin N. Lightfoot, Transport Phenomena, Revised 2nd edition, John Wiley & Sons, Inc, New York, 2007.

[44] S.S. Rathore, B. Mehta, P. Kumar, M. Asfer, Flow characterization in triply periodic minimal surface (TPMS)-based porous geometries: part 1—Hydrodynamics, Transp. Porous. Media 146 (3) (Feb. 2023) 669–701, https://doi.org/10.1007/S11242-022-01880-7.

[45] S.J.P. Callens, C.H. Arns, A. Kuliesh, A.A. Zadpoor, Decoupling minimal surface metamaterial properties through multi-material hyperbolic tilings, Adv. Funct. Mater. 31 (30) (Jul. 2021), https://doi.org/10.1002/ADFM.202101373.